The final publication is available at

https://doi.org/10.1016/j.advwatres.2018.03.013

Additional Information

A Numerical Study of the Complex Flow Structure in a Compound Meandering Channel

Ignacio J. Moncho-Esteve[a] (*Corresponding Author*), Manuel García-Villalba[b], Yasu Muto[c], Koji Shiono[d], Guillermo Palau-Salvador[a]

[a]*Dept. of Rural and Agrifood Engineering, Hydraulic Division, Universitat Politècnica de València, Camino de Vera s/n, 46022 Valencia (Valencia), Spain*
igmones@doctor.upv.es
Tlf.: 0034-629936415
Fax: 0034-963877549

[b]*Bioeng. and Aeroespace Eng. Dept. Universidad Carlos III de Madrid. 28911 Leganés (Madrid), Spain*
manuel.garcia-villalba@uc3m.es

[c]*Faculty of Science and Technology, Tokushima University, Tokushima, Japan.*
muto_yas@ce.tokushima-u.ac.jp

[s]*School of Architecture, Building and Civil Engineering, Loughborough University, Loughborough, United Kingdom*
shiono4511@gmail.com

ABSTRACT

In this study, we report large eddy simulations of turbulent flow in a periodic compound meandering channel for three different depth conditions: one in-bank and two overbank conditions. The flow configuration corresponds to the experiments of Shiono and Muto (1998). The predicted mean streamwise velocities, mean secondary motions, velocity fluctuations, turbulent kinetic energy as well as mean flood flow angle to meandering channel are in good agreement with the experimental measurements. We have analyzed the flow structure as a function of the inundation level, with particular emphasis on the development of the secondary motions due to the interaction between the main channel and the floodplain flow. Bed shear stresses have been also estimated in the simulations. Floodplain flow has a significant impact on the flow structure leading to significantly different bed shear stress patterns within the main meandering channel. The implications of these results for natural compound meandering channels are also discussed.

Keywords: Turbulence, Flow Structure, Large Eddy Simulation, Meander, Flooding

1 Introduction

A deep understanding of the turbulent structures associated with the flow through compound meandering channels is of immense interest to river engineers. Such turbulent structures affect significantly the transport of sediments, solutes and pollutants in rivers. Therefore, in order to develop strategies to handle and regulate rivers (e.g. river restoration, navigation, water quality, etc.) it is important to understand how and when these structures are formed, and what effects they cause. The watercourse of a natural river is often characterized by a curvy shape. The curves or meanders consist of an inner bank and an outer-bank. Meanders are formed when river flow erodes the outer-banks of the channel. As a result of the complex geometry of the waterway, the resulting flow structure is highly three-dimensional, exhibiting secondary motions. Moreover, river flows in a compound channel often inundate the adjacent plains, which generate more complicated flow structures between the in-bank and the floodplain flows.

Compared with the extensive knowledge for straight compound channel flows, see for example Xie et al. (2013) and references therein, less information is available for compound meandering channel flows. Field measurements in a compound natural channel have been reported by Carling et al. (2002). Experimental, laboratory studies using natural cross-sectional shapes have been reported by, among others, Wormleaton et al. (2004), Shiono et al. (2008, 2009a, 2009b) and Mera et al. (2015). From these studies, it is often difficult to systematize the acquired knowledge due to the complex geometry and high variability of the studied waterways, as well as those found in nature. To gain physical insight it is often beneficial to study simplified geometries, as in the experiments of Shiono and Muto (1998). With respect to modelling, in the literature there are several Reynolds-averaged Navier–Stokes (RANS) studies of flow in compound meandering channels (Morvan et al., 2002; De Marchis and Napoli, 2008; Shukla and Shiono, 2008; Jing et al., 2009). However, Van Balen et al. (2010), Constantinescu et al. (2013) and Moncho-Esteve et al. (2017) have shown that, generally, Large Eddy Simulation (LES) provides better results than RANS in curved open-channel turbulent flows. An additional advantage is that using LES it is possible to obtain further physical insights from the computed data. Indeed, the intention of this work is to complement the experimental work of Shiono and Muto (1998) by perfoming LES of the same flow configuration with rectangular cross-section and straight flood plain banks.

Secondary motions in meanders were first mentioned more than 150 years ago by Boussinesq (1868) and Thomson (1876). The structure of the secondary motions and its influence on the streamwise velocity distribution as well as on mixing have been discussed, among others, by Blanckaert and Graf (2004), Blanckaert (2009) and Moncho-Esteve et al. (2017). The secondary motions depend strongly on the waterway geometry; they are affected both by the sinuosity of the channel as well as by the cross-sectional shape. One or several counter-rotating cells may be observed. The most important one is often called centre-cell or primary vortex. It is located far from the banks and occurs due to the imbalance between the driving centrifugal force and the transverse pressure gradient. The imbalance introduces a flow from the outer to the inner-bank at the bottom of the channel and a flow from the inner to the outer-bank at the surface of the channel. This is the reason why the sediments are mainly transported from the outer to the inner-bank (Julien and Duan, 2005). The structure of the secondary motions is affected by the inundation of the adjacent plains. It has been observed that the secondary flow structures in meandering channels have an opposite sense of rotation of the primary vortex at bend apexes before and after inundation (Shiono and Muto, 1998). This is because, when inundation is

1 present, the primary vortex is generated by the floodplain flow crossing over the main channel
2 flow in the crossover region.

3 Shiono and Muto (1998) also characterized the turbulence in meandering channels with and
4 without inundation. They found that, without inundation, the highest levels of turbulence were
5 found near the wall, while with inundation the turbulent intensities just below the bankfull level
6 become more important. This is a consequence of the strong shear layer formed in the crossover
7 region at the interface between the floodplain flow and the in-bank flow. However, they were
8 not able to measure bed shear stresses. High bed shear stresses are directly related to bed
9 erosion and, often, indirectly linked to regions of high turbulent levels, and, as a consequence,
10 these regions are the sites of enhanced mixing of nutrients and pollutants. Bed shear stresses are
11 difficult to measure experimentally, but they can be easily estimated from the LES results.
12 Thus, the main aim of this study is to provide a more complete picture of the flow in compound
13 meandering channels by analyzing the relation between secondary motions, turbulent kinetic
14 energy and bed shear stresses.

15 The paper is structured as follows. A brief description of the experiments of Shiono and Muto is
16 provided in section 2. In section 3, the numerical method and the computational setup are
17 presented. The results are presented in section 4. First, the mean streamwise flow is presented in
18 cross-sections, followed by the mean flow angle and the velocity fluctuations. The mean
19 secondary flow structure is presented by providing cross-sectional views and three-dimensional
20 visualizations. In section 4.5, the bed shear stresses are estimated and discussed in terms of their
21 relation to the mean flow structure. The results section ends with a brief discussion of the
22 implication of the results for natural flow configurations. Some conclusions are drawn in section
23 5. Note that preliminary results for one of the cases presented here were reported in Moncho-
24 Esteve et al. (2010).

2   Experimental Cases

26 In this study we use, as reference, the experiments of Muto (1997) and also reported by Shiono
27 and Muto(1998). The experimental flume of rectangular cross-section consisted of five
28 meanders, where the bends were connected by straight sections (Fig. 1). All the measurements
29 were carried out under a quasi-uniform flow condition that was defined as when the deviation of
30 the water-surface slope from the bed slope became less than 2%. The central radius of channel
31 curvature r_c was 0.425 m and the arc of meander Φ was 120° with the corresponding sinuosity
32 $s=1.370$ ($s = L/L_w$, being L the curved channel bend length and L_w the meander wavelength).
33 The width of the meandering channel b was 0.15 m and the channel depth h was 0.053 m. More
34 details of the case are specified in Table 1. The velocity measurement was carried out with 2-
35 component laser-Doppler anemometer (LDA) and flow visualization at the water surface using
36 solid tracers and a fixed camera technique.
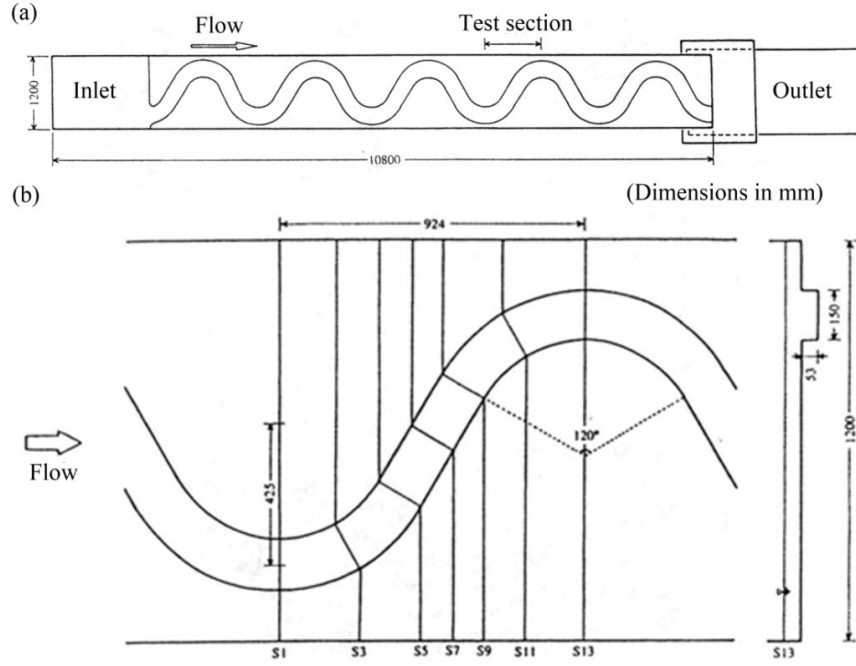
s = 1.370, rectangular channel

Fig. 1. (a) Set-up of the experimental flume. (b) Meandering channel configuration for the test section. Adapted from Muto (1997). (*1.5-colum fitting image*)

Table 1. Meander parameters for tested channel.

Angle of arc	Meander wavelength	Total width	Width of meander	Bend radius	Crossover length	Crossover angle	Sinuosity	Channel width	Depth of meander
Φ (°)	L_w (mm)	B (mm)	B_w (mm)	r_c (mm)	L_{co} (mm)	θ (°)	s	b (mm)	h (mm)
120	1848	1200	900	425	376	60	1.37	150	53

Water depth conditions for simulations were one in-bank case and two overbank cases, namely $Dr = 0.15$ and $Dr = 0.50$, where Dr is the relative depth defined in Table 2. These were chosen because the secondary flow structure in the main channel, and the shearing mechanisms between the main channel flow and the flood plain flow, were of particular interest. Measurements were conducted at section numbers 1, 3, 5, 7, 9, 11 and 13 (Fig. 1). The hydraulic conditions of the selected cases are specified in Table 2.

Table 2. Hydraulic conditions of the experiments of Muto (1997) selected for the LES.

Depth condition	Discharge	Water Depth	Relative depth	Relative depth	Mean velocity	Friction velocity[a]	Reynolds number[b]	Froude number[c]
Dr	Q ($\cdot 10^{-3} \text{m}^3\text{s}^{-1}$)	H (m)	H/h	$Dr=(H-h)/H$	U_s (ms^{-1})	u_* (ms^{-1})	Re ($\cdot 10^3$)	Fr
Bankfull	1.556	0.0519	0.969	---	0.197	0.0148	21.9	0.359
0.15	2.513	0.0630	---	0.15	0.129	0.0120	6.60	0.340
0.50	19.996	0.1059	---	0.495	0.282	0.0221	49.20	0.401

a. $u_* = (gRS)^{1/2}$, where g = gravity acceleration, R = hydraulic radius and S = energy slope

b. $Re = 4U_sR/v$, where v = kinematic viscosity, R = hydraulic radius

c. $Fr = U_s(gR)^{-1/2}$

3   Numerical Method and Computational Setup

The simulations were performed with the in-house code LESOCC2 (Large Eddy Simulation On Curvilinear Coordinates). It is a successor of the code LESOCC developed by Breuer and Rodi (1996) and it is described by Hinterberger (2004). The code solves the Navier-Stokes equations on body-fitted, curvilinear grids using a cell-centred finite volume method with collocated storage arrangement for the Cartesian velocity components. Second-order central differences are employed for the convection as well as for the diffusive terms. The time integration is performed with a predictor-corrector scheme, where the explicit predictor step for the momentum equations is a low-storage three-stage Runge-Kutta method. The corrector step covers the implicit solution of the Poisson equation for the pressure correction (SIMPLE). The Rhie and Chow momentum interpolation (Rhie and Chow, 1983) is applied to avoid pressure-velocity decoupling. The Poisson equation for the pressure increment is solved iteratively by means of the "strongly implicit procedure" of Stone (Stone, 1968). Parallelization is implemented via domain decomposition, and explicit message passing is used with two halo cells along the inter-domain boundaries for intermediate storage.

The subgrid-scale (SGS) stresses, resulting from the unresolved motions, are modelled using the Smagorinsky subgrid-scale model (Smagorinsky, 1963) with a model constant C_s of 0.1. Such an approach has been used successfully for similar flows by Hinterberger et al. (2007) and Moncho-Esteve et al. (2017). For flows without homogeneous directions, as the present one, the Smagorinsky model is more robust than other models like the dynamic Smagorinsky which require some kind of smoothing of the model parameter (like time relaxation). Near the walls Van-Driest damping is employed.

For the numerical calculation a global coordinate system was used (X, Y, Z), while for the data analysis the quantities were transformed on a body-fitted coordinate system. According to the definition in Shiono and Muto (1998), the x-axis is hereby along the centreline of the channel bed, the y-axis along the span-wise and the z-axis along the vertical direction. The computational grids consisted of $\sim 5.8 \cdot 10^6$ grid points for the Bankfull case, $\sim 7.2 \cdot 10^6$ for the $Dr = 0.15$ case and $\sim 12.1 \cdot 10^6$ for the $Dr = 0.50$ case. More details of the grids are specified in Table 3.

Table 3. Computational grids for the simulated cases.

Case	Used Mesh: Grid Points in x-, y-, z-	Total Grid Points
Bankfull	$1200 \cdot 110 \cdot 44$	5,808,000
$Dr = 0.15$	$960 \cdot 90 \cdot 40 = 3,456,000$ (in-bank) $960 \cdot 390 \cdot 10 = 3,744,000$ (flood plain)	7,200,000
$Dr = 0.50$	$960 \cdot 90 \cdot 40 = 3,456,000$ (in-bank) $960 \cdot 390 \cdot 23 = 8,611,200$ (flood plain)	12,067,200

(a)

Bankfull

(b)

$Dr = 0.15$

(c)

$Dr = 0.50$
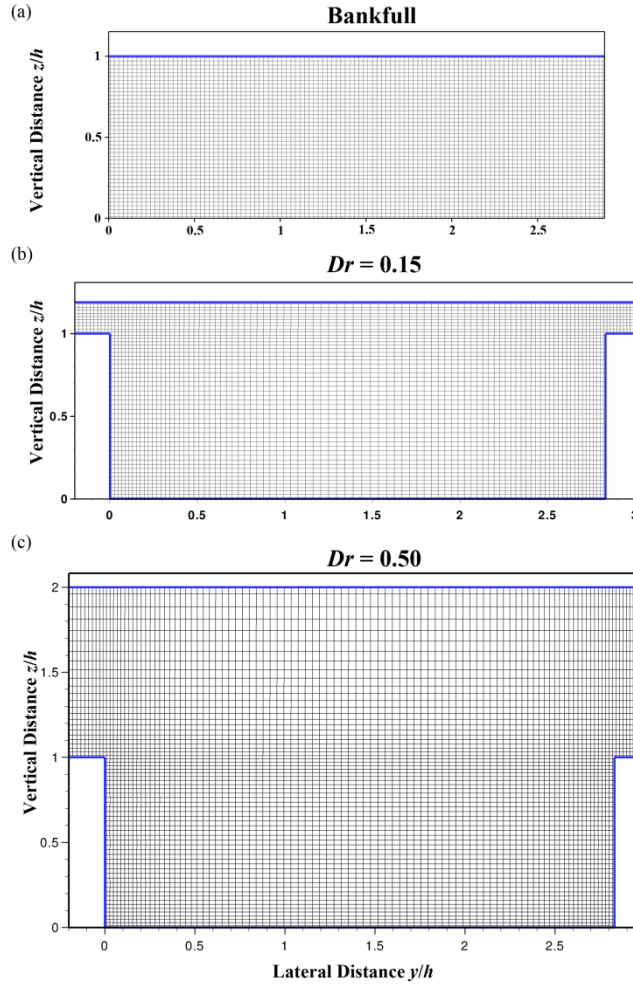

Lateral Distance *y/h*

Fig. 2. Detail of the grids in a cross section of the compound meander used in the LES simulations. (a) bankfull case, (b) $Dr = 0.15$ case and (c) $Dr = 0.50$ case. (*1.5-colum fitting image*)

The computational grids are uniform along the centreline in *x*-direction and stretched in *y*- and *z*-directions to achieve a better resolution of the near wall motions. The grid sizes in terms of wall units near the walls ($\Delta y^+ = \Delta z^+$) and the maximum value of Δx^+ in the stream-wise direction are shown in Table 4 for each one of the computational cases. The stretching ratio is kept to a fix value of 1.03 in all cases. A view of the grid cross section for each of the cases is shown in Fig. 2. Only one wavelength of meander was computed and periodic boundary conditions were defined in the entrance and exit of the meander. A no-slip condition, with smooth surface, was implemented at the bottom boundary and lateral walls jointly with the Werner-Wengle wall model. In this way, with the wall function of Werner and Wengle (1993) the shear friction at the first cell near the wall is calculated using the 1/7th-power law of the instantaneous velocities. Moreover, a rigid-lid assumption was used for the free surface, which means that a symmetry condition is introduced, whereby the velocity normal to the surface and the velocity gradient parallel to the surface are set to zero; hence, the surface is approximated by a free-slip rigid surface. This method has been successfully employed in previous studies of similar configurations (Stoesser et al., 2008; Brevis et al., 2014 and Moncho-Esteve et al., 2017). The employed grid resolution is reasonable for a non-wall-resolving simulation. This is supported by the good agreement with experimental data that will be shown in the following

sections. For comparison, Xu et al. (2013) employed a similar grid resolution in their meandering open channel bend calculations while Brevis et al. (2014) employed a somewhat finer grid resolution for a similar flow configuration. In addition, the grid resolutions employed here are somewhat finer than those employed in a previous study by some of the present authors (Moncho-Esteve et al., 2017). In the latter case the agreement with experimental data was also good. Therefore, we are confident that the grid resolution employed here is good enough to study the mean flow and turbulence characteristics of the flow under consideration.

Table 4. Grid sizes in terms of wall units near the wall (Δy^+ and Δz^+) and maximum grid sizes in stream-wise direction (Δz^+).

| Case		Δx^+	Δy^+	Δz^+
Bankfull		29	12	12
$Dr = 0.15$	in-bank	32	9	9
	flood plain	30	12	12
$Dr = 0.5$	in-bank	52	15	15
	flood plain	44	16	16

4   Results & Discussion

4.1   *Streamwise Flow*

All the velocities in this section are normalized by the average velocity $U_s = Q/A$, Q being the flow rate and A being the transverse section of the flume. The Figure 3 presents a qualitative comparison of the mean streamwise velocity $\langle u \rangle$ for the Bankfull, $Dr = 0.15$ and $Dr = 0.50$ cases, where angular brackets $\langle \rangle$ denote average over time. For the sake of brevity, only Section No. 09 is shown for comparison with the experimental data. In general a good agreement was found between simulations and experiments at the meandering cross-sections. In this figure the results of the simulations are shown on the left and the experimental results on the right.

In the Bankfull case (Fig. 3, top panels) the highest velocities, with a magnitude over $1.3U_s$, are found near the inner bank (convex channel wall) in the bend apex (not shown). As the flow advances towards the second half of the curve, the core of the maximum velocity moves towards the outer bank (concave channel wall), and the distribution of the velocity are softened. In the middle of the crossover region of the meander a flow region superior to $1.2U_s$ reaches the outer wall (not shown). After the flow enters the second curve (Section No. 09) the maximum velocity is still moving towards the right sidewall. This tendency matches the experimental data accurately. Coinciding with the previous studies (Chang, 1971; Moncho-Esteve et al., 2017) the maximum value of the streamwise velocity seems to be placed in the entrance of the curve, near the Section No. 09, where values over $1.3U_s$ are reached. Overall, a correct consistency in both shape and intensity on the contours of the mean streamwise flow is appreciated, although the simulation underestimates slightly the values compared to the experimental results.

For the $Dr = 0.15$ case (Fig. 3, middle panels) regions of high velocity are formed near both walls in the apex of the curve (not shown), while the central part is occupied by a lower velocity area. Throughout the meander, large regions can be found in which the velocity is higher than U_s. This suggests that the flow in the meander with a low flood water depth still maintains a dominant longitudinal component (Shiono and Muto, 1998). At the bend apex (not shown), areas of slower flow motion can be seen near the bed in the middle section, which are clearly

1   influenced by the secondary flow structures through the meander (see Fig. 10 and corresponding
2   discussion). Moreover, in the crossover region (Section No. 05-09), a steep velocity gradient
3   related to the flow entering from the upstream flood plain is developed in the vertical direction
4   near the bankfull level. This area develops laterally as it proceeds in the crossover region. The
5   mean flow patterns described are observed in both the contours from the simulations and from
6   the experiments. The agreement between the two is good, although there is a small
7   overprediction of the maximum velocities in the simulation. Comparing the contours in *Bankfull*
8   and *Dr* = 0.15 cases (Figs. 3, top and middle panels), it can be observed that even a low flood
9   water depth influences significantly the flow patterns within the meander. This is particularly
10   clear in the crossover region.

11
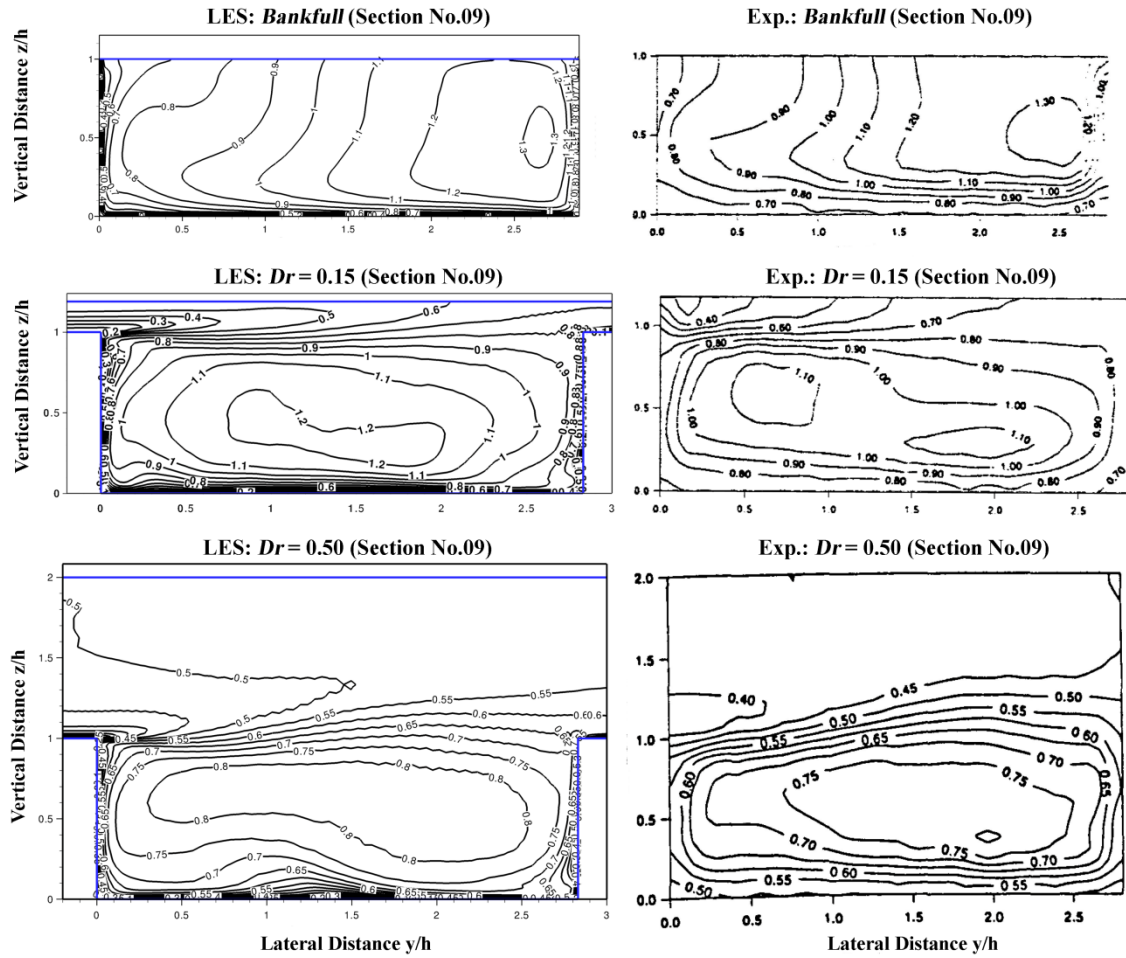
Fig. 3. Mean streamwise velocity $\langle u \rangle / U_s$ in the Bankfull (top panels), *Dr* = 0.15 (middle
panels) and *Dr* = 0.50 (bottom panels). Left: LES simulation; Right: experimental
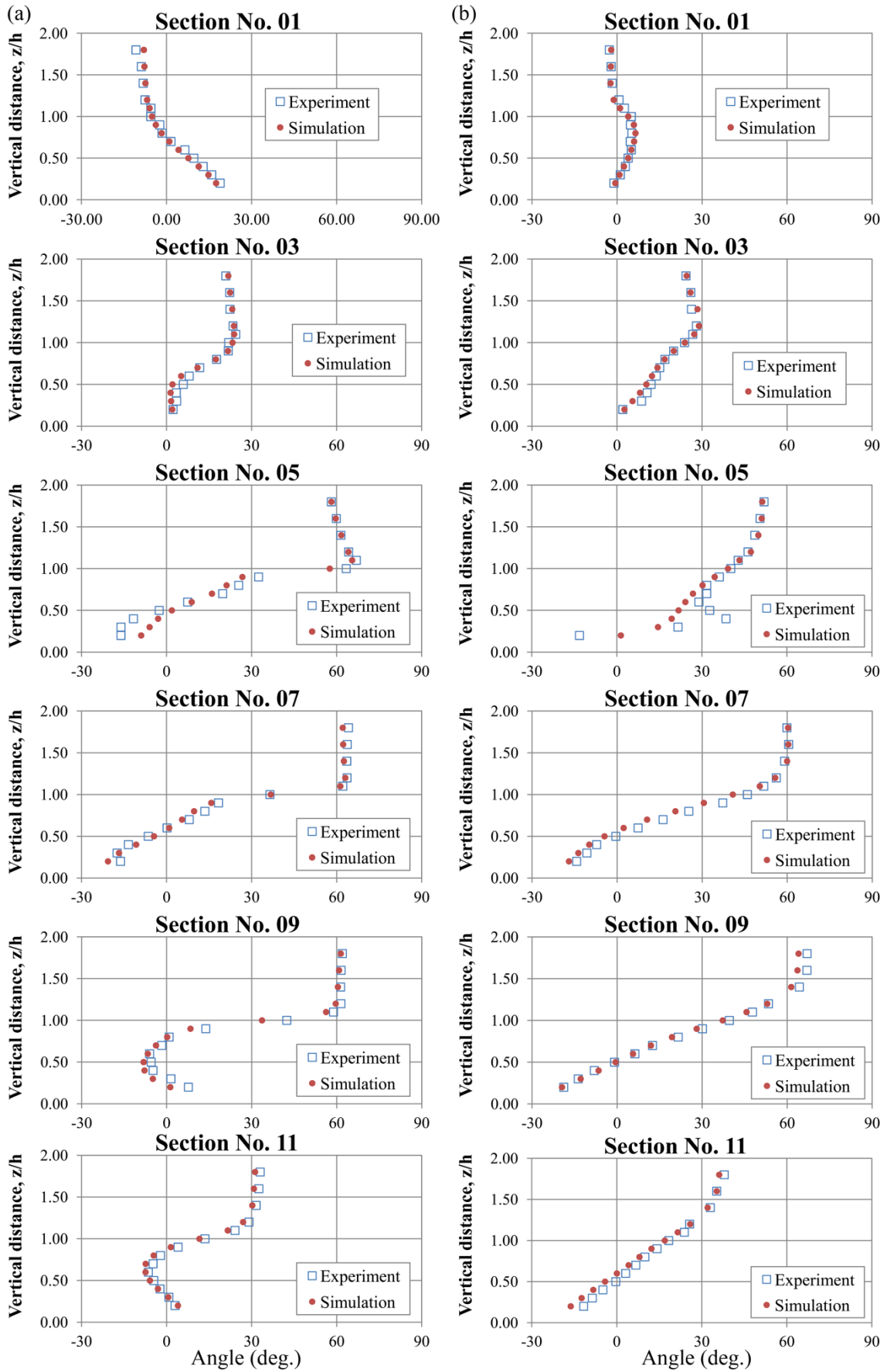measurements by Muto (1997). (*2-colum fitting image*)

15

16   Regarding the case *Dr* = 0.50 (Fig. 3, bottom panels), in the crossover region of the meander,
17   and on top of it, a velocity gradient can also be observed, due to the inflow from the floodplain
18   into the meander. It can be seen an area of considerable low velocity in the right-hand wall of
19   the outlet of the curves (Sections No. 03 and No. 5 (not shown)). Moreover, the in-bank flow
20   has a streamwise velocity value throughout the meander channel under U_s, which suggests that,
21   with high levels of flooding, a dominance of the floodplain flow over the meander ensues
22   (Shiono and Muto, 1998). There is a good correlation between the simulation and the

8

experimental features described above. Similar to the $Dr = 0.15$ case, the velocity value in the simulation seems to be slightly overestimated. Comparing $Dr = 0.15$ and $Dr = 0.50$ cases (Figs. 3, middle and bottom panels), it is noteworthy that the flow patterns within the meander ($z/h<1$) are rather similar, however, the velocity levels are different. While with the low water depth (Fig. 3, middle panels) the velocities within the meander may be higher than U_s, with the high water depth (Fig. 3, bottom panels) the velocities are significantly lower. As Shiono et al. (2008, 2009a, 2009b) demonstrated, sediment transport rate decreases from in-bank flow to $Dr = 0.3$ which means that in the meandering channel the velocity decreases as well.

Some deviations between the experimental data and the simulation results are found near the free surface. This might be due to the use of the rigid-lid assumption for the free surface. Besides, in the simulation some wiggles can be observed in the sections where there is supposed to be a strong flow interaction between the meander flow and the flood plain flow (Sections No. 05 and No. 09). This indicates that a somewhat finer resolution might have been required to avoid these oscillations, especially in the region of the interface between meander and flood plain. However, since the overall agreement with the experimental data is very good we can infer that the impact of the wiggles is minor. Finally, recall from Fig. 1 that sections 1 and 13 (not shown) present mirror symmetry with respect to the midline of the cross section since these sections are the opposite apices of the periodic meander. This mirror symmetry indicates that the simulations have been run long enough for the statistics to converge.

4.2 *Flood Flow Angle*

Fig. 3 have provided a qualitative comparison between experiments and simulations. A quantitative comparison is provided in Fig. 4. This is done by resolving the floodplain flow into two components as it was done by Shiono and Muto (1998), see their Fig. 7. The angle between these two components, $\theta,$ can be obtained as $\theta = \tan^{-1}(\langle v \rangle / \langle u \rangle)$, where $\langle v \rangle$ is the mean lateral velocity and $\langle u \rangle$ the aforementioned mean streamwise velocity. Shiono and Muto (1998) reported vertical profiles of the flow angle for the case $Dr = 0.50$ at two spanwise locations, $y/h = 0.56$ (inner side of the meander channel) and $y/h = 2.55$ (outer side). Fig. 4 displays these profiles at several sections, including both experimental data and simulation results. Shiono and Muto (1998) stated that especially at $y/h = 2.55$, Sections No. 05 and 09, the mean flow angles do not coincide with the meander channel angles (60º). The authors indicate that the main channel fluid runs into the flood plain. On the other hand, the mean flow angles at Sections No. 01, 03 and 05 are less than the channel angles (0 º, 30 º and 60 º respectively), which indicates that the floodplain flow is diverted into the main channel flow direction. However, the angles at Sections No. 09 and 11 (60 º and 30 º) are greater than the channel angle, representing a flood plain flow diversion outwards towards the flood plain. These features related with the expansion and contraction (i.e. a phenomenon showed by Kiely, 1990) of the flood plain flow entering and escaping respectively from the main channel flow are shown and clarified in the next sections.

(a)

Section No. 01

Section No. 03

Section No. 05

Section No. 07

Section No. 09

Section No. 11

(b)

Section No. 01

Section No. 03

Section No. 05

Section No. 07

Section No. 09

Section No. 11

Fig. 4. Mean flood flow angle to meandering cannel with depth variation for Dr = 0.50, (a) y/h = 0.56, (b) y/h = 2.55. (*2-colum fitting image*)

1   As it can be seen in Fig. 4, the predicted mean flow angle profiles show very good agreement

2   with the measurements. Although the trends of the profiles are to a large extent reproduced by

3   the model, significant differences were found in the in-bank flow of Section No. 05, specially in

4   the outer side of the meander (y/h = 2.55). In this section, the largest discrepancies with respect

5   to the measured flow angle are 19.15 deg. at z/h = 0.4. In the inner side of the meander channel

6   (y/h = 0.56), the major differences were found in the same section at z/h = 0.3. The deviation

7   may stem from the steep gradient that exists in this region, related with the aforementioned

8   entering and escaping flow as well as the complex secondary motions due the flood plain flow.

9   However, in general the good agreement with the flow angle supports the assumption that the

10   grid resolution is sufficient to capture major effects in the mean flow field.

11   ### 4.3 *Fluctuations and Turbulent Kinetic Energy*

12   The root mean square of the streamwise and lateral velocity fluctuations, $\langle u' \rangle$ and $\langle v' \rangle$

13   respectively, were obtained and compared with the experimental measurements (Muto, 1997). A

14   prime denotes velocity fluctuation. Statistics were collected during 500 dimensionless time units

15   H/U_s. In the following velocity fluctuations are normalized with the friction velocity u_*. The

16   calculated u_* for each experimental case is listed in Table 2. The simulations were performed

17   using a horizontal water surface and a horizontal channel bed. This is a general technique used

18   in CFD to model flow in channels. The driving force is a pressure gradient, instead of the

19   gravity. Thus, in the case of the simulations, the friction velocity was obtained as

20
$$(u_*)_{sim.} = \left(\frac{1}{\rho} \frac{dp}{dx} R \right)^{1/2} \tag{1}$$

21   where ρ is the density, p is pressure and R is the hydraulic radius. The values obtained for the

22   Bankfull, Dr = 0.15 and Dr = 0.50 simulations were 0.0166, 0.0116 and 0.0210 ms^{-1}

23   respectively, which are reasonably consistent with the experimental ones (Table 2).

24   Figures 5 and 6 present a qualitative comparison of the velocity fluctuations for the Bankfull,

25   Dr = 0.15 and Dr = 0.50 cases. For the sake of brevity, only Section No. 09 is shown. For the

26   other sections a similar agreement was found between simulations and experiments.

27   In the Bankfull flow (Fig. 5, top panels), $\langle u' \rangle$ reaches values up to 3 u_* along the inner bank of

28   the bends (not shown). Besides, another area of high $\langle u' \rangle$ appears near the channel bed and to a

29   lesser extent next to the outer banks. The later is not found in the experimental data, most

30   probably due to the resolution near the walls. Regarding the lateral component $\langle v' \rangle$ (Fig. 6, top

31   panels), large values appear at the channel centre near the water surface in the curves, where it

32   is about 2 u_*. Generally, a correct consistency in both shape and intensity on the contours of the

33   streamwise and lateral velocity fluctuations is appreciated, although the simulation

34   underestimates slightly the experimental results.
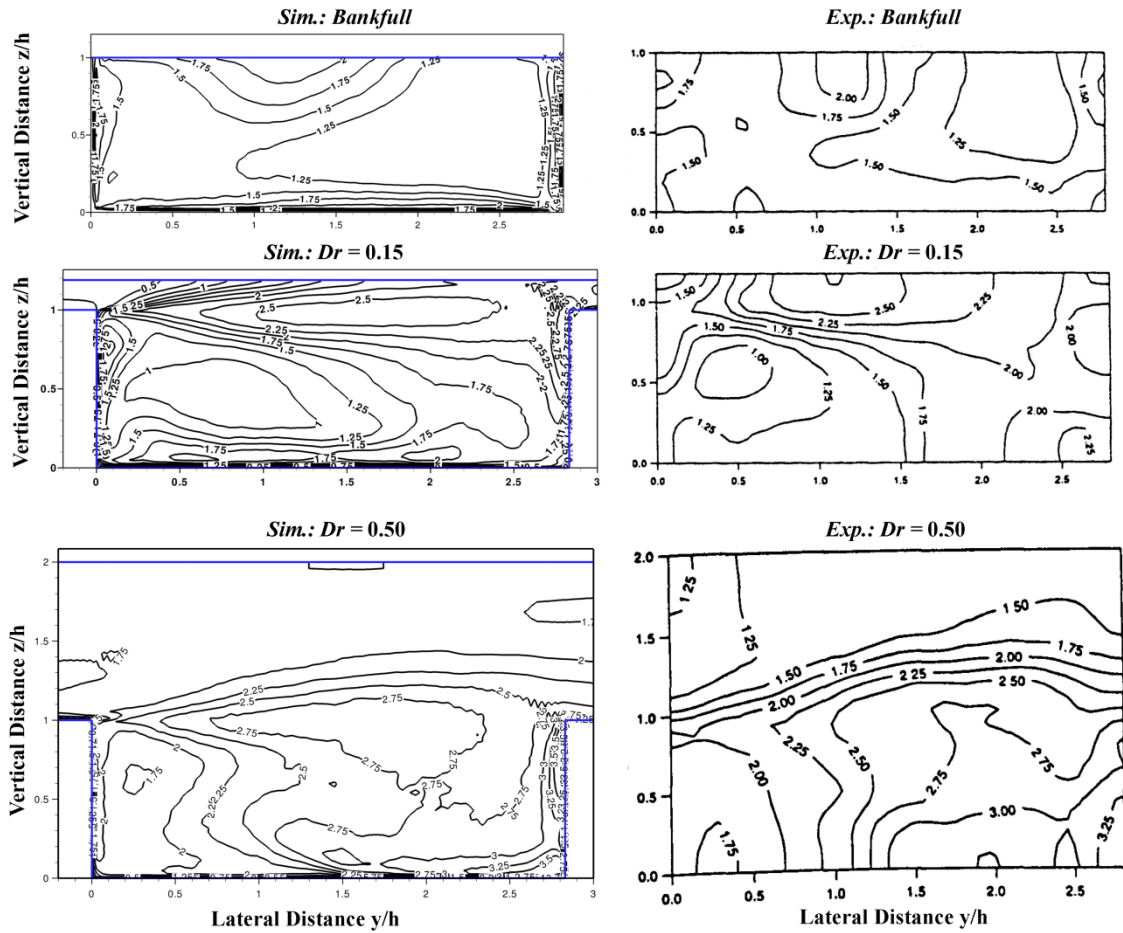
Fig. 5. Contours of the root mean square streamwise velocity fluctuations $\langle u' \rangle$ normalized with the u_* in Section No. 09 for the Bankfull (top), $Dr = 0.15$ (middle) and $Dr = 0.50$ (Bottom). Left: LES simulation; Right: experimental measurements by Muto (1997). (*2-colum fitting image*)

In the $Dr = 0.15$ case (Fig. 5 and 6, middle panels) the results show a good agreement with the experimental results by Muto (1997) except near the water surface. The maximum values are around 2.25 u_* and they appear in shear layer regions where the flow interaction occurs by the floodplain flow entering the main channel in the upper left corner of Sections No. 05-09. This interaction is also well reproduced by the LES results. This area is developed over the channel width, increasing in size. In addition, both the shape and magnitudes of $\langle u' \rangle$ and $\langle v' \rangle$ correspond well with each other in most of the cross-section.
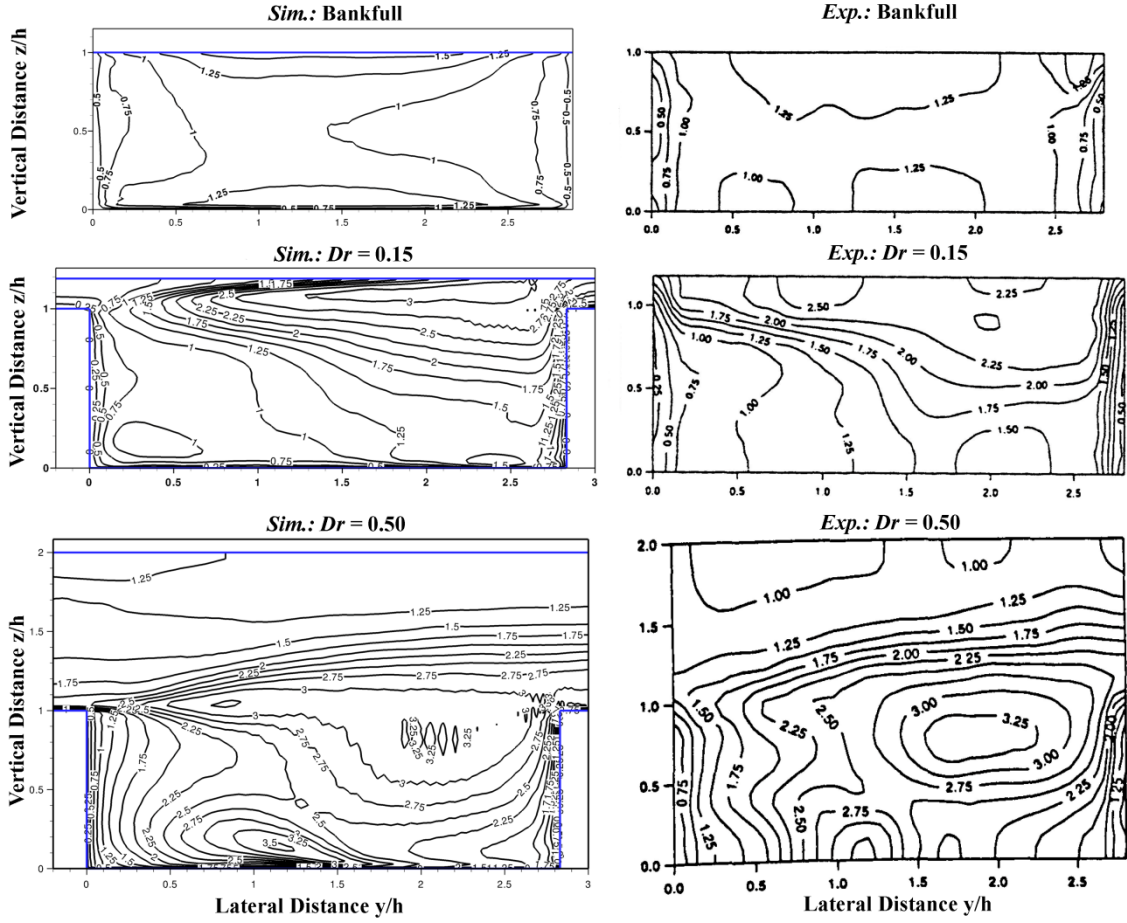
Fig. 6. Contours of the root mean square lateral velocity fluctuations $\langle v' \rangle$ normalized with the u_* in Section No. 09 for the Bankfull (top), $Dr = 0.15$ (middle) and $Dr = 0.50$ (Bottom). Left: LES simulation; Right: experimental measurements by Muto (1997). (*2-colum fitting image*)

In the case of $Dr = 0.50$ (Fig. 5 and 6, bottom panels), the upper layer flow seems to influence significantly the turbulent flow structure. For this water depth condition, the lower layer is more turbulent than the upper layer, which is clearly seen in the crossover region. The area of large turbulent intensities expands slightly into the upper layer, with values over 2.5 u_*. For both velocity components, this area of high turbulent intensity is found roughly at the same central location. Although the velocity fluctuations seem to be slightly overestimated in the simulations, the patterns described above are qualitatively similar in both the experimental data and the simulations results. Like for the mean streamwise velocity components (Fig. 3, bottom panels), some small wiggles can be observed in the sections where there is a strong flow interaction between the meander flow and the flood plain flow (Sections No. 05 and No. 09).

As Muto (1997) noticed, the turbulent shear layer generated at the bankfull level is most dominant for the bankfull flow ($Dr = 0.15$ and $Dr = 0.50$ cases), leading to a high turbulence intensity, both in streamwise direction and laterally and, accordingly, both $\langle u' \rangle$ and $\langle v' \rangle$ reflect such a feature.

Moreover, in this section, a qualitative comparison of the turbulent kinetic energy k is provided in Fig. 7 and 8 between the cases Bankfull, $Dr = 0.15$ and $Dr = 0.50$. Only Sections No. 01, 05, 09 and 13 are shown for comparison. The turbulent kinetic energy is given by

$$k = \frac{1}{2}\left(\left\langle u'^{2} \right\rangle + \left\langle v'^{2} \right\rangle + \left\langle w'^{2} \right\rangle \right) \tag{2}$$

Since in the experiments the vertical component was not measured in the whole area of the cross sections (Muto, 1997), only the data from the simulations is presented. In the following k is normalized with the square of the friction velocity $u_*^{\,2}$.

In the Bankfull case (Fig. 7, left panels), the highest values of k are found near the side walls and the bed of the channel, due to the strong shear found in these regions. Also the level of turbulence is higher near the free surface than in the core of the channel. Although it is difficult to observe in the figure, the maximum value of k reaches values about 6.9 u_*^2. As mentioned before, Sections No. 01 and 13 should present mirror-symmetry with respect to the midline and indeed the patterns obtained from the simulations are almost symmetric.
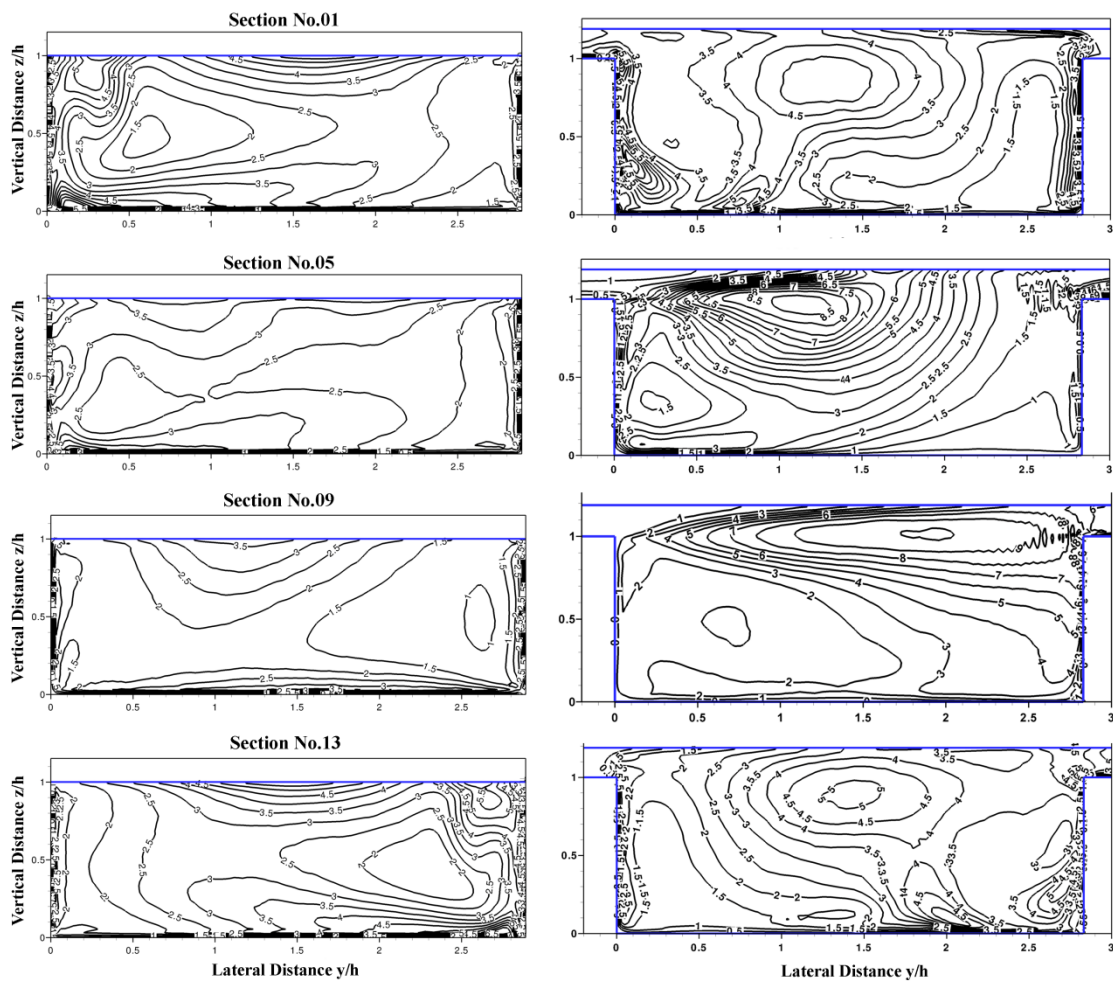
Fig. 7. Turbulent kinetic energy k normalized with the $u_*^{\,2}$ in the Bankfull simulation (Left) and the $Dr = 0.15$ simulation (Right). (*2-colum fitting image*)

In the case $Dr = 0.15$ (Fig. 7, right panels) the area where the higher turbulence values are gathered is located in the upper part of the meander through its straight section, corresponding to the interaction between the inner and the outer flows. This is particularly clear in Section No. 09, where a region of hight turbulence level is found near the meander top ($z/h \sim 1$). Values higher than 9.0 u_*^2 are reached. It is possible to notice that in the bed, near the outer banks of the

14

1   curves (right lateral wall at Sections No. 01 and 05 and left lateral wall at Sections No. 09 and
2   13), areas with k lower than 1.5 u_*^2 appear. Just as Muto (1997) noted, due to the secondary
3   flow being very weak in this area (as will be shown below), deposit of sediments in natural beds
4   can occur.

5   For $Dr = 0.50$ (Fig. 8), a similar behaviour to the $Dr = 0.15$ case is observed, keeping the core of
6   maximum k slightly under the level of the floodplain bank and taking more space. The
7   maximum values surpass in this case 13 u_*^2. Throughout the crossover region (see Section No.
8   05), high values of k can be seen in the flood plain flow, near the outline of the curve ($y/h = 3$,
9    $z/h \sim 1$).

10   Regarding the distribution of k, one of the key differences between the $Dr = 0.15$ and $Dr = 0.50$
11   cases is the position of the core of the turbulent area. In the shallow overbank flow, this area
12   remains close to the water surface, but nevertheless in the deep flooding case it is located mostly
13   below the bankfull level, $0.5<z/h<1.0$. The study of Muto (1997) did not clarify whether the
14   former's characteristic was related to the depth conditions or whether it could be due to the
15   fairly shallow flooding depth which was not enough to give a proper measurement resolution in
16   the vertical direction. The fact that this feature was well drawn by the numerical results leads us
17   to state a clear correlation with the water depth and this turbulent core.

Section No.01

Section No.05

Section No.09
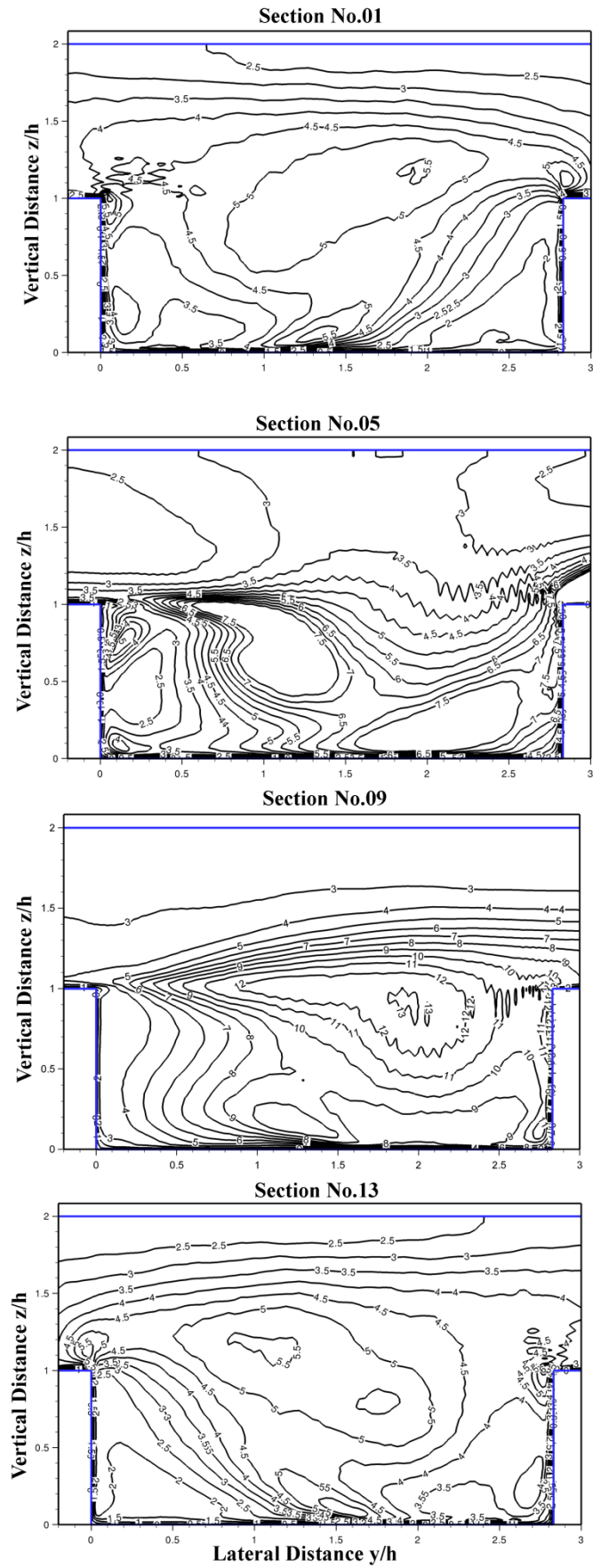
Section No.13

Fig. 8. Turbulent kinetic energy k normalized with the u_*^2 in the $Dr = 0.50$ simulation. (*2-colum fitting image*)

16

$Dr = 0.50$

$Dr = 0.15$

Bankfull

$k/(u_*)^2_{sim.}$
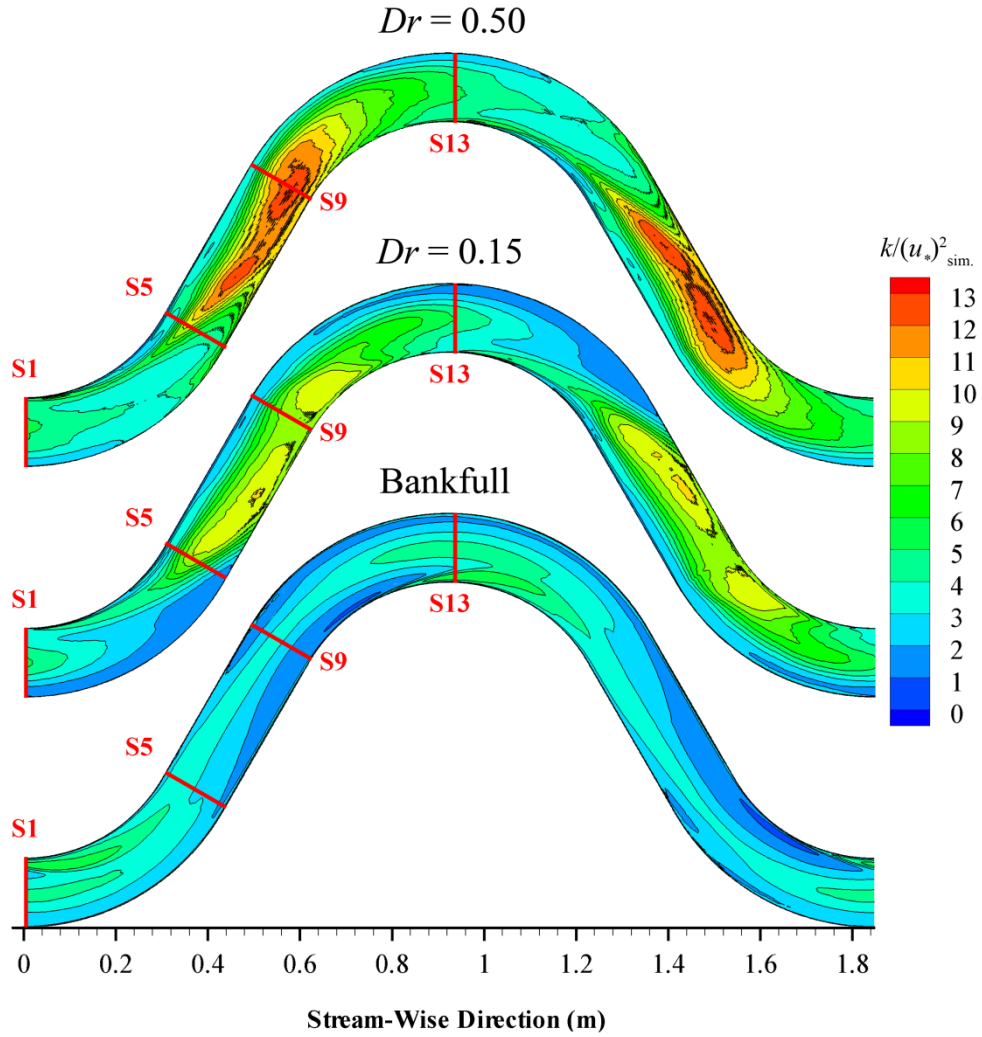
Fig. 9. Turbulent kinetic energy k normalized with the u_*^2 in a horizontal plane ($z/h = 0.9$) of the meandering channel. Top: $Dr = 0.50$ case, middle: $Dr = 0.15$ and bottom: Bankfull. (*Colour should be used in print*) (*2-colum fitting image*)

Figures 7 and 8 show that the floodplain flow changes the structure of the turbulent kinetic energy patterns near the interface with respect to the bankfull case. Therefore, it is interesting to study the longitudinal patterns near this interface. Figure 9 shows the contours of the normalized turbulent kinetic energy in a horizontal plane ($z/h = 0.9$) of the main channel for the Bankfull, $Dr = 0.15$ and $Dr = 0.50$ cases. The corresponding sections shown in the previous Figs. 7 and 8 are specified here for better interpretation. In the case of Bankfull, the maximum values of k appear near the bend apices of the meander. As mentioned by Muto (1997), these values are related to the wall generated turbulence and the secondary flow generated turbulence, both of which contribute mainly to the production of $\langle u' \rangle$ and $\langle v' \rangle$ respectively. However, in case of flooding, the region with the highest k appears in the crossover region. This effect has a higher intensity for $Dr = 0.50$ than for $Dr = 0.15$. In this area a very intense shear layer between the flow in the flooding level and the flow throughout the meander is produced. This shear layer generates additional turbulence due to the interaction and the mixing process between the flooding flow and the meandering flow. In the case $Dr = 0.15$ a great influence in the wall generated turbulence and the secondary flow in the meander must still exist, considering, as

17

1 Muto (1997) indicated, the k is related in the crossover region with the distribution of $\langle u' \rangle$ and

2 $\langle v' \rangle$. On the other hand, in the case of $Dr = 0.50$ the level of turbulence rises and the main

3 contribution to the production of turbulent energy appears near the shear layer, which is more

4 correlated with the $\langle v' \rangle$ (Muto, 1997) due to the crossing of the flooding flow over the

5 meandering flow.

6 The aforementioned flow intrusion and the resultant interaction between the upper and lower
7 flows strongly affect the flow structure in compound meandering channels during floods (Muto,
8 1997). Specifically, this relates to the internal shear at the bankfull level for overbank flows,
9 which in turn is the dominant mechanism for turbulence generation in these cases. Moreover,
10 this feature induces the horizontal layer of turbulence nature in the crossover region, which is
11 the main factor for production of secondary flows. The results showed here (Fig. 9) cover the
12 shape and form of such turbulent shear layer for the two water depths.

13   4.4   *Secondary Flow*
14 The mean secondary current vectors of Sections No. 01, 03, 05, 07, 09, 11 and 13 are presented
15 in Figs. 10 and 11 for the Bankfull, $Dr = 0.15$ and $Dr = 0.50$ cases.

16 For the in-bank flow case (Fig. 10, left panels), a big clockwise circulation cell can be observed
17 near the inner bank (left lateral wall) at Section No. 01. This secondary current comes from the
18 previous bend and it is similar in form and magnitude as the one shown at Section No. 13.
19 While the flow near the bed moves from the outer to the inner-bank (right to left), the flow close
20 to the surface moves in the opposite direction. In addition to the centre-region cell a small cell
21 near the outer-bank (right lateral wall) is present, rotating in an anti-clockwise direction. The
22 flow at the bottom of the channel has already switched sign at Section No. 11. In this position,
23 the small outer-bank cell rotating in anti-clockwise direction mentioned above becomes the
24 centre-region cell. Close to the surface of the inner bank, rotating in a clockwise direction, the
25 previous centre-region cell can be seen decreasing in strength. This behaviour seems to confirm
26 that these secondary currents are a process of the growth and decay of two cells of the primary
27 vortex, which has been also shown and discussed in Moncho-Esteve et al. (2017), for a similar
28 flow configuration. The agreement (comparison not shown) with the experimental results
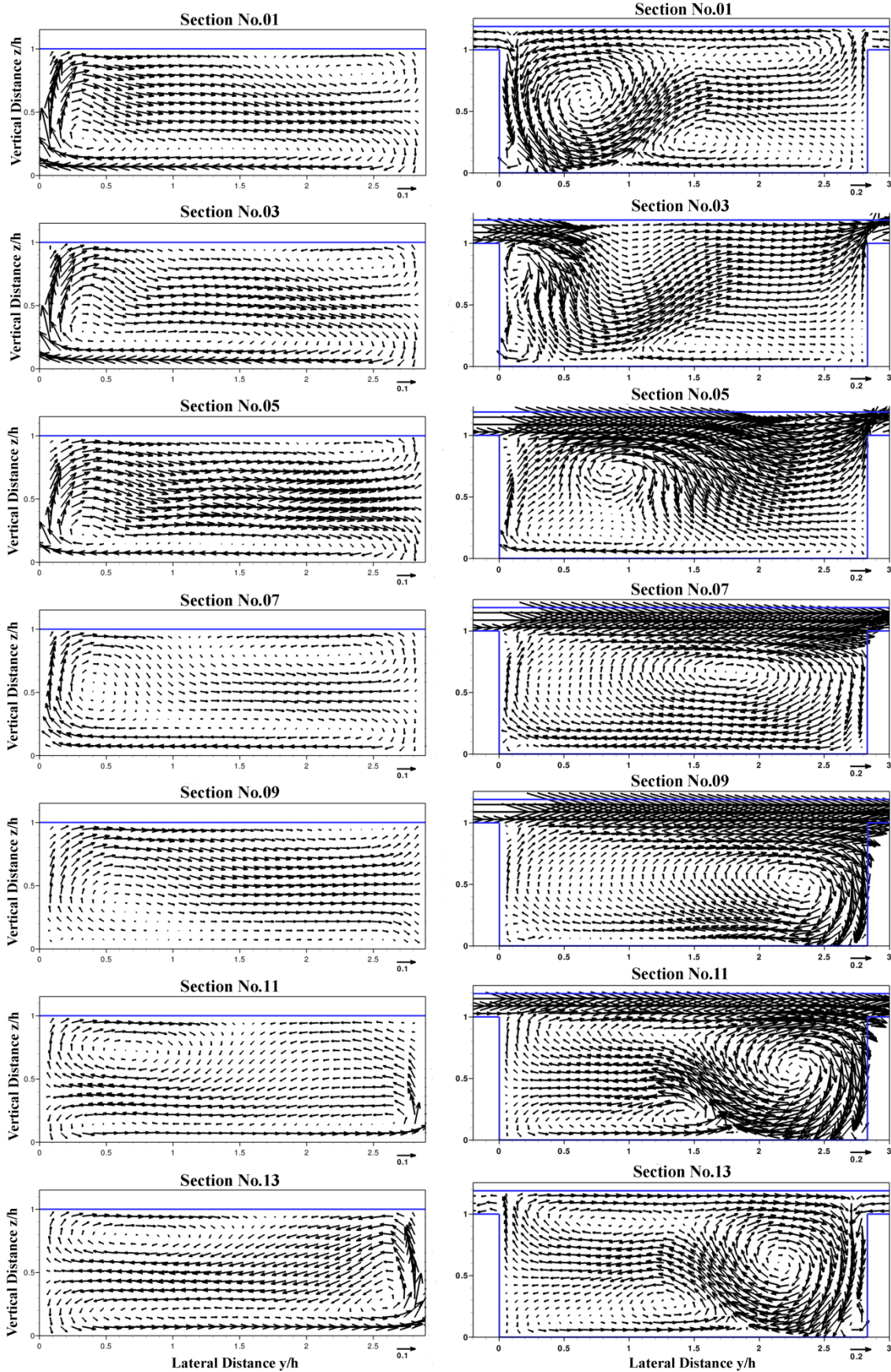29 (Muto, 1997) is remarkably good.

Fig. 10. Mean secondary flow vectors in the Bankfull simulation (Left) and *Dr* = 0.15 simulation (Right). (*2-colum fitting image*)

The effect of the floodplain flow completely changes the mechanisms of the secondary currents within the meander. For the $Dr = 0.15$ case (Fig. 10, right panels), a big shear-generated anti-clockwise recirculation cell could be observed at Section No. 01 in the vicinity of the inner bank which comes from the previous bend; this recirculation is weakened by the centrifugal effects throughout the bend. In this case, a small counter clockwise cell is also noticeable at the outer bank and near the channel bed. However, both circulations disappear suddenly along the next reach by entering floodplain flow that changes completely the secondary circulation patterns inside the meander. In order to evaluate where this transition takes place additional cross-sections were studied (results not shown). These sections represent the point where the aforementioned big shear-generated recirculation cell, which was generated in the previous bend, disappears completely. Fig. 12a shows the additional cross-sections between which the transition occurs for the case $Dr = 0.15$. Thus, the change occurs at an angle of roughly 24º from the bend apex. At this moment, the meander flow takes an oblique direction to the main floodplain stream, which produces a high velocity above the bankfull level in the crossover region and a vigorous expansion-contraction phenomenon occurs when the floodplain flow enters into the meander section and vice versa. From that section on (namely Section No. 02.9), a big clockwise centre-region cell appears (from Section No. 05 to 09 in Fig. 10, right panels). This big secondary current progresses downstream towards the inner wall of the next bend (Section No. 09). In the latter part of the meander, as the meander takes a parallel direction to the floodplain mainstream, the floodplain flow entering the meandering channel decreases and a counter rotation cell appears, similar to Section No. 01. The progress of the primary vortex generated by the floodplain flow along the meandering channel is very well predicted by the LES simulation (comparison with the experiments of Muto not shown). The fact that the secondary circulations within the meandering channel change completely as soon as there is some floodplain flow can be understood by simple analogy with the flow in a lid driven cavity (Koseff and Street, 1984). While the flow along the meander has the same direction as the floodplain flow, the secondary patterns are little affected. As soon as the orientation of the meander changes sufficiently, the floodplain flow acts as a driving mechanism for the secondary currents, imposing their rotation.
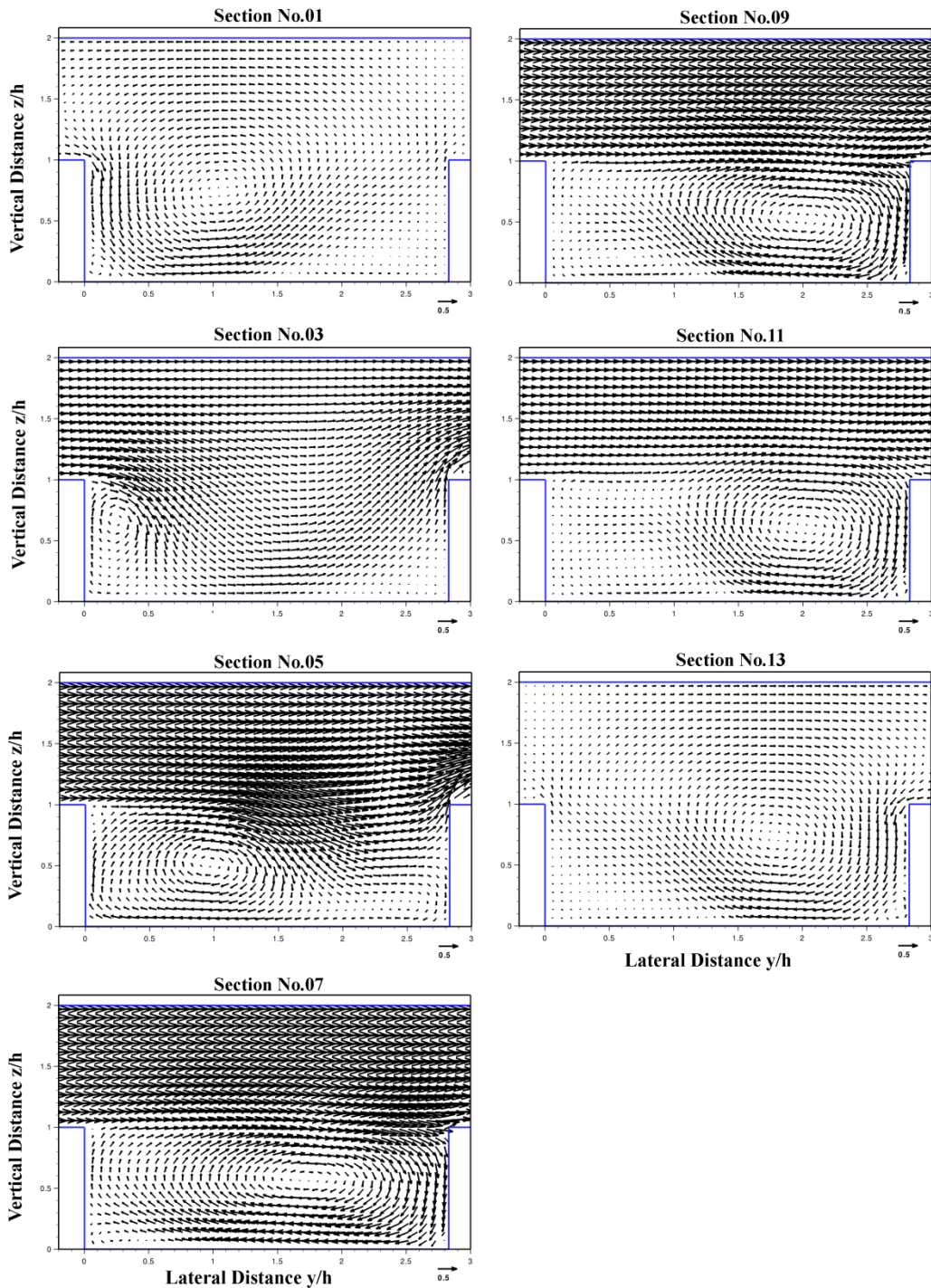
**Fig. 11.** Mean secondary flow vectors in the *Dr* = 0.50 simulation. (*2-colum fitting image*)

For the *Dr* = 0.50 case (Fig. 11), the flow behaves in a simpler way because the influence of the cross-over flow of the floodplain mainstream is more pronounced. At Section No. 01, almost no recirculation cell is noticeable. However, at an angle of 16º (see Fig. 12b), a big centre-cell recirculation begins to be formed by the entrance of floodplain flow. Thus, almost the whole cross-sectional area is occupied by only one dominant secondary flow cell which displaces its centre towards the inner bank at Sections No. 07 and 09. From that section on, the secondary flow decays and it has almost vanished at Section No. 13. The expansion and contraction processes are also visible around Section No. 05. The situation is similar although not so marked as regards to the *Dr* = 0.15 case. The progress of the primary vortex generated by the

21

floodplain flow along the meandering channel is once again very well predicted by the LES simulation (experimental data of Muto not shown).
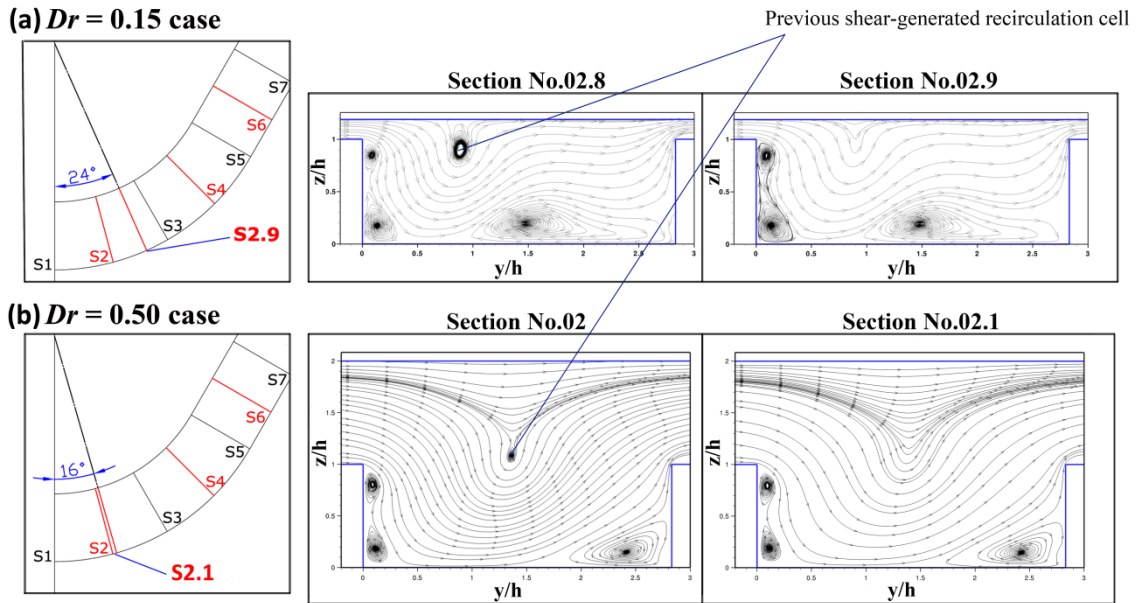

Fig. 12. 2D-streamtraces in additional cross-sections where entering floodplain flow cancelled completely the previous shear-generated vortex inside the meander. (a) Dr = 0.15 case, (b) Dr = 0.50 case. (*2-colum fitting image*)

In Fig. 13 and 14, different views of the three-dimensional streamlines of the mean flow are shown for the Dr = 0.15 and 0.50 cases. The streamlines are coloured with the normalized turbulent kinetic energy. This figures illustrate the phenomenon of the interaction and mixing process between the floodplain mainstream and the in-bank meandering flow, whose consequences are mainly the horizontal shearing and the downstream effects of crossover flow. These pictures confirms the tendency (Shiono and Muto, 1998) of the flow within the main channel below the bankfull level to follow the meander channel, while above the bankfull level it tends to follow the valley direction. As it can be seen, the flow enters the meander (expansion behaviour) in the inner margin of the bends and begins to swirl according to the secondary currents previously explained. It is also noticeable how the contraction (escaping flow) phenomenon occurs near the outer bank of the bends when the flow from the main channel reaches the floodplain again before the interaction with the meander flow. The latter two features are in agreement with the description of Sellin et al. (1993), who showed velocity vectors in the main channel and the flood plain along a compound meander channel and pointed out the dropping and recirculation of the upper flow in the main channel. In the case of the Dr = 0.15, it can be seen how the main floodplain flow seems to be more conditioned (significant deflection is shown) by the in-bank secondary flow through the straight section, whereas in Dr = 0.50 case it appears to flow smoothly over the main channel, which means that with a deep condition the interaction is less important and the two layers are less dependent on each other. In both cases and according to the Figs. 7 (right panels) and 8, higher values of the turbulent kinetic energy can be seen in the middle of the crossover region of the meander and the entrance of the curves (Section No. 09). Moreover, the contribution of the turbulent kinetic energy seems to concentrate within the main meandering channel for Dr = 0.15 more than in the floodplain. On the other hand, greater turbulence values are gathered not only under the level of the floodplain bank and taking more space but also throughout the flood plain for Dr =0.50.
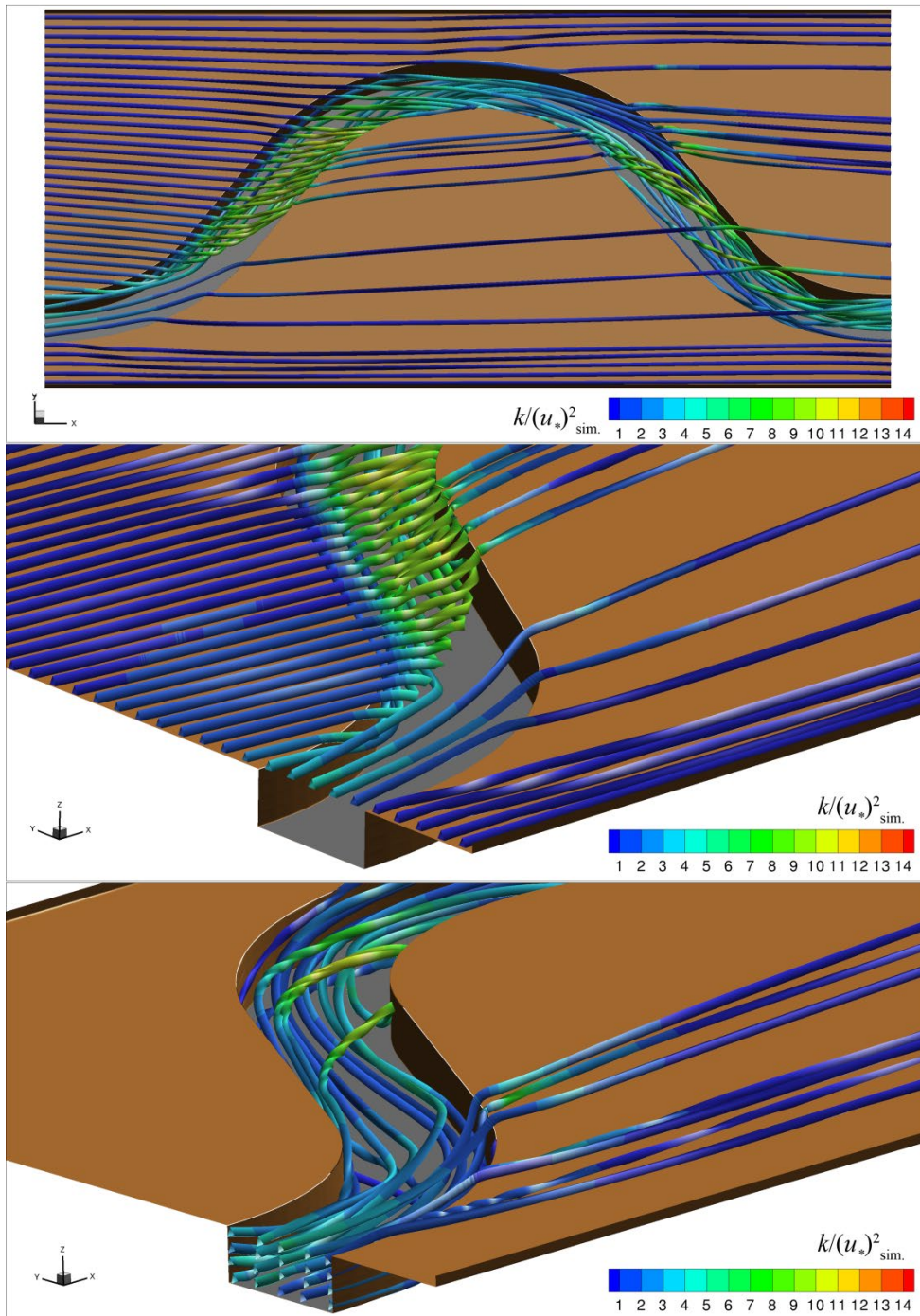
Fig. 13. Different views of the 3D stream traces of the mean flow coloured with the normalized turbulent kinetic energy $k/(u_*)^2_{sim.}$ for $Dr = 0.15$ case. (*Colour should be used in print*) (*1.5-colum fitting image*)
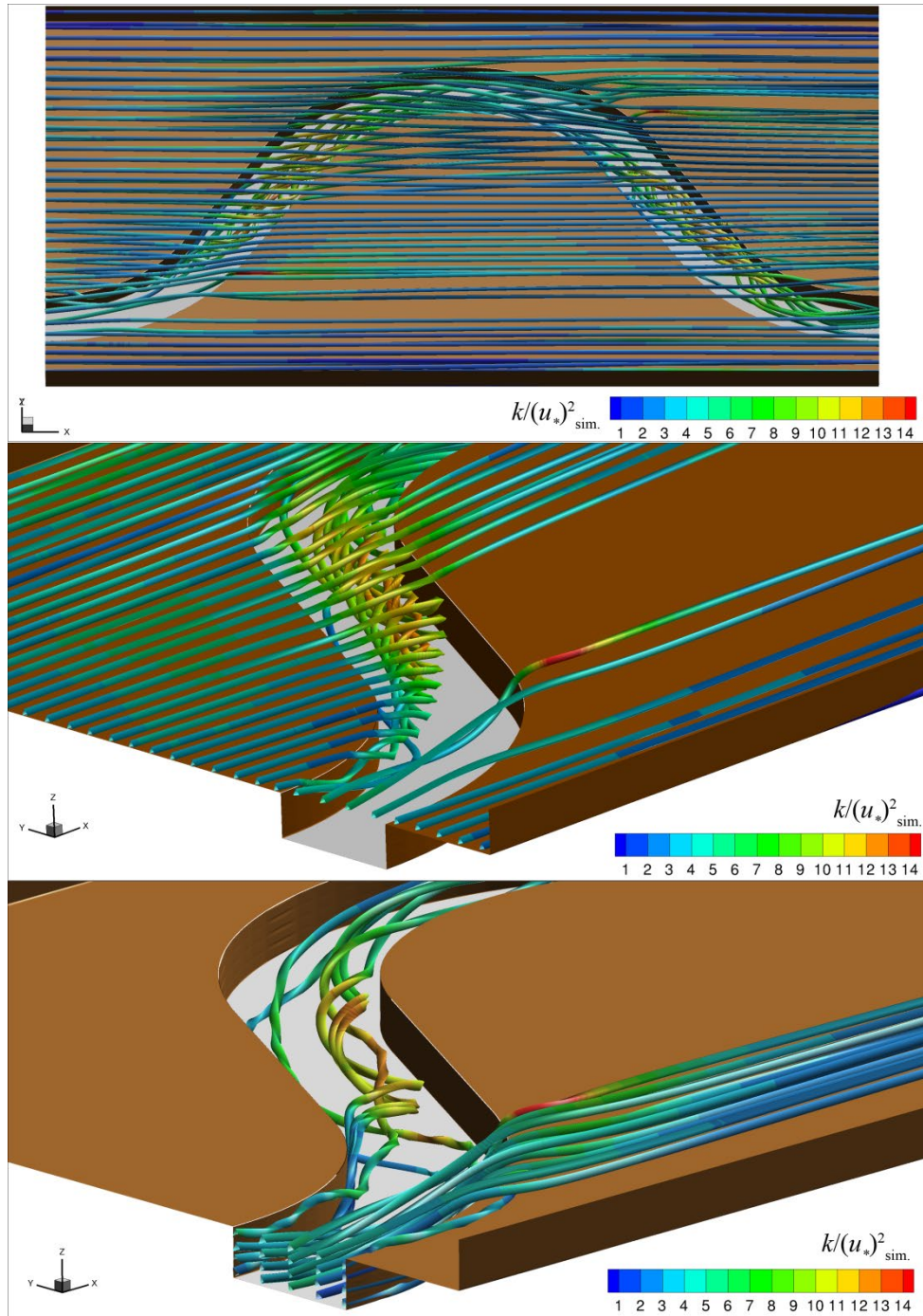
Fig. 14. Different views of the 3D stream traces of the mean flow coloured with the normalized turbulent kinetic energy $k/(u_*)^2_{sim.}$ for $Dr = 0.50$ case. (*Colour should be used in print*) (*1.5-colum fitting image*)

A detailed analysis of this process is illustrated in Fig. 15. The figure shows some plots of the mean flow vectors and the normalized turbulent kinetic energy $k/(u_*)^2_{sim.}$ near the outer side of the meander channel and the flood plain edge roughly in Section N. 05, for $Dr = 0.15$ and $Dr = 0.50$ cases. A small recirculation pattern appears around Section No. 05 (Fig. 15, middle panels) at the floodplain edge region. The pattern seems to be bigger for $Dr = 0.50$ (Fig. 15b) compared with the $Dr = 0.15$ case (Fig. 15a). This indicates that when the flood water depth increases, this

24

1   interaction between the flooding and the main channel meandering flow increases. An area
2   producing high turbulent energy is easily recognized in the vicinity of the recirculation (Fig. 15,
3   top panels), over the flood plain bank and near the concave side of the meander wall. This
4   energy reach values up to 13 u_*^2 for the $Dr = 0.15$ and exceeds 29 u_*^2 in the $Dr = 0.50$ case. A
5   similar turbulent area was noticed by Muto (1997) by means of the depth averaged turbulent
6   kinetic energy on the flood plain next to the bend exit. Muto also summarized the findings of
7   Imamoto and Fujii (1975), who stated that turbulence becomes more intense when the flow
8   passes over a forward step, being this tendency more noticeable near the bed; our results agree
9   with their results and support the evidence that this highly turbulent fluid comes from the main
10   channel. Moreover, the mean flow vectors at the flood plain edge (Fig. 15, bottom panels)
11   follow the path towards the edge of the outer bank of the meander channel. This trend occurs in
12   both cases ($Dr = 0.15$ and $Dr = 0.50$) in a narrow area alongside the floodplain edge region.
13   This area corresponds to the aforementioned recirculation and ranges from the second half of
14   the bend (between Section No. 03 and No. 05) to the first part of the crossover region (between
15   Section No. 05 and No. 07). This area agrees with the vigorous expulsion of the inner channel
16   water (contraction process) described by Ervine et al. (1994) and Wormleaton et al. (2004),
17   which induces the recirculation (Fig. 15, middle panels) and the consequent tendency of vectors
18   to move towards the edge of the outer bank. This highly turbulent mechanism, not seen before,
19   could be related to the erosion mechanisms (producing strong scour in this zone) and the
20   channel migration present in this kind of flow. Although the intensity of the vectors appears to
21   be qualitatively similar in both cases (Fig. 15, bottom panels), recirculation and turbulence are
22   greater for $Dr = 0.50$ (Fig. 15d). In this sense, for higher levels of flooding, a bigger influence of
23   this mechanism in the scouring process is expected.
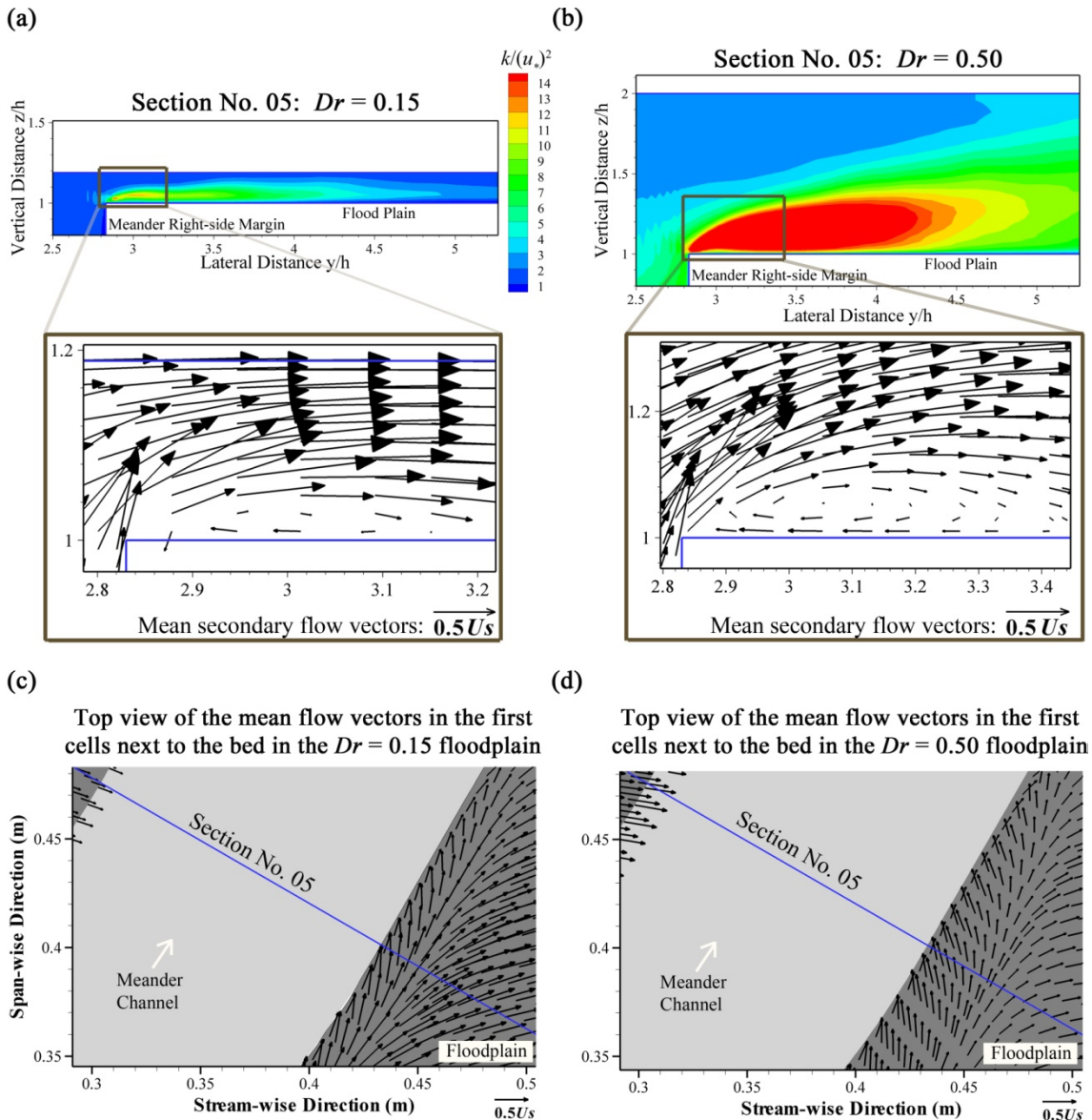
Fig. 15. Detail of the outer side of the meander channel near Section N. 05. Top: normalized turbulent kinetic energy $k/(u_*)^2_{sim.}$. Middle: close up view of the mean secondary flow vectors. Bottom: top view of the mean flow vectors in the first cells next to the floodplain bed. (a, c) Dr = 0.15 case, (b, d) Dr = 0.50 case. (*2-colum fitting image*)

Although there are clear significant differences in the flow configuration, the aforementioned phenomenon of flow expansion (flow entering from the flood plain into the meander channel) could be related to a separation of flow such as those produced by dune formation (Shiono et al., 2008; Stoesser et al., 2008). In this process, the flow over the dune crest creates a large separation zone, with which is associated a turbulent free shear layer generating large scale eddies that travel through the flow domain. In our cases, this behaviour appears to weaken when the flood increases (Dr = 0.50). In the Dr = 0.50 case, the mean flow is more likely to just travel over the meandering flow, generating an in-bank flow structure with a primary gyre which is more similar to the one observed in the flow around an emerged dead zone sequence (Brevis et al., 2014; Weitbrecht, 2004). However, at a depth near Dr = 0.50, Shiono et al. (2008) showed dunes which were caused by a number of secondary flows in sequence along the meandering channel. On the other hand, the phenomenon of contraction (escaping flow from the meander

26

onto the flood plain) near the cross-over region could be connected to the flow behaviour over the cylinder top. Hain et al. (2008) and Palau-Salvador et al. (2010) studied in depth the flow around finite-height cylinders and showed that the flow separates at the leading edge, yielding a recirculation. In fact, the flow picture over the cylinder top sketched by the last mentioned authors (Fig. 16 in Palau-Salvador et al., 2010) is quite similar as the one showed in this study (Fig. 16).

4.5   *Bed Shear Stress*

In natural rivers, the bed shear stress is important in determining the bed erosion and the sediment transport (Shan et al., 2016). The bed shear stress is hardly ever measured in experiments because of the inherent measurement difficulty; however, it is easier to obtain from the computational data. This section therefore presents the bed shear stress at the bottom walls as an application of the initial step in the erosion processes. To do this, we estimate this parameter in the first cells of the mesh next to the bed in the meander and floodplain making use of the equation

$$\langle \tau_w \rangle = \mu \frac{du_t}{dn} \tag{3}$$

where, μ is the dynamic viscosity, u_t is the mean tangential velocity component at the bed and n the distance from the bed. The bed shear-stress is normalized with the total bed shear stress obtained from the resulting pressure gradient

$$\tau_t = R \frac{dp}{dx} \tag{4}$$

where R is the hydraulic radius. As a cautionary note, recall that the present simulations are not wall-resolving. This means that the bed shear stress values discussed below can be only considered as an estimation of the real values. We believe, however, that the trends and differences observed between the three cases are reliable, and would differ little if obtained with wall resolving simulations.

Fig. 16 shows the distribution of the normalized bed shear stress of the Bankfull case. Note that for brevity the shear stress is not shown in the meandering lateral walls, although its value is not negligible. The maximum value of the bed shear stress occurs in the curves, close to the inner bank, reaching values of up to $0.9\tau_t$. In the downstream flow direction, the shear stress is shifted and smoothed towards the outer edge of the curves. In the straight sections a small area of maximum shear appears at the right margins, just outside the curves.

Fig. 17 shows the distribution of the normalized bed shear stress in the $Dr = 0.15$ case, both in the meander and in the floodplain. Within the meander, an effect similar to the Bankfull case occurs, reaching values up to $0.9\tau_t$. However, very low shear zones (almost $0.0\tau_t$) appear in the left margins of the straight sections, and in the central areas of the curves near the inner banks, coinciding with low velocity zones in the bed. Likewise, in the floodplain the greatest bed shear stresses of the domain occur, reaching values up to $1.1\tau_t$. The maximum values are concentrated in the zones where there is a greater interaction between the meander flow and the floodplain flow, which has its origin in the strong acceleration due to the contraction and expansion of the flow. As was pointed out by Wormleaton et al. (2004), the great expulsion of

1 the flow in this case induces local high velocities near the main channel outer bank, which are
2 related to the risk erosion in that area.

3 Finally, in the *Dr* = 0.50 case (Fig. 18), the maximum bed shear stresses of the entire domain
4 are produced within the meander, reaching values higher than $1.1\,\tau_t$. The maximum values
5 occur, unlike in previous cases, in the straight sections of the meander, occupying much of the
6 bed due to the big center-cell originated by the flow coming from the floodplain. At the exit of
7 the curves of the meander, large areas of low shear (almost $0.0\,\tau_t$) occur in the outer margins,
8 due to the low velocities in these sections. Within the floodplain, the bed shear stresses appear
9 to be concentrated below the meander margins that lie downstream of the flow direction of the
10 flooded plane, although their contribution is much lower than in the shallow case. The effects of
11 bed shear stress seem to be more intense within the meander as the level of flooding increases.
12 In this case and, as we mentioned earlier, the influence of the expulsion of water on to
13 floodplain is less than in the *Dr* = 0.15 case. On the other hand, as was illustrated by
14 Wormleaton and Ewunetu (2006), in deep floodplain, a strong shear-driven recirculation
15 through the meandering crossover region can cause deep scour in this area.
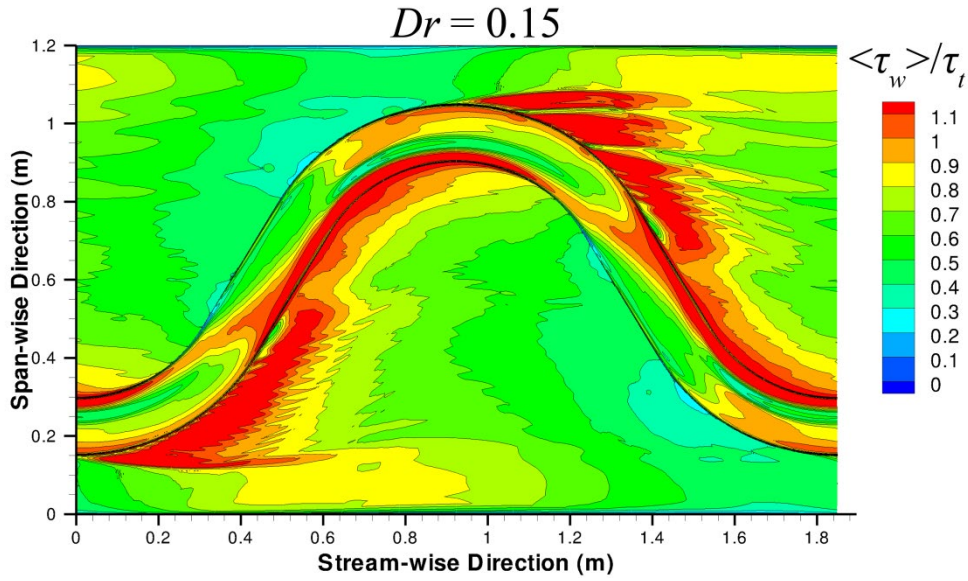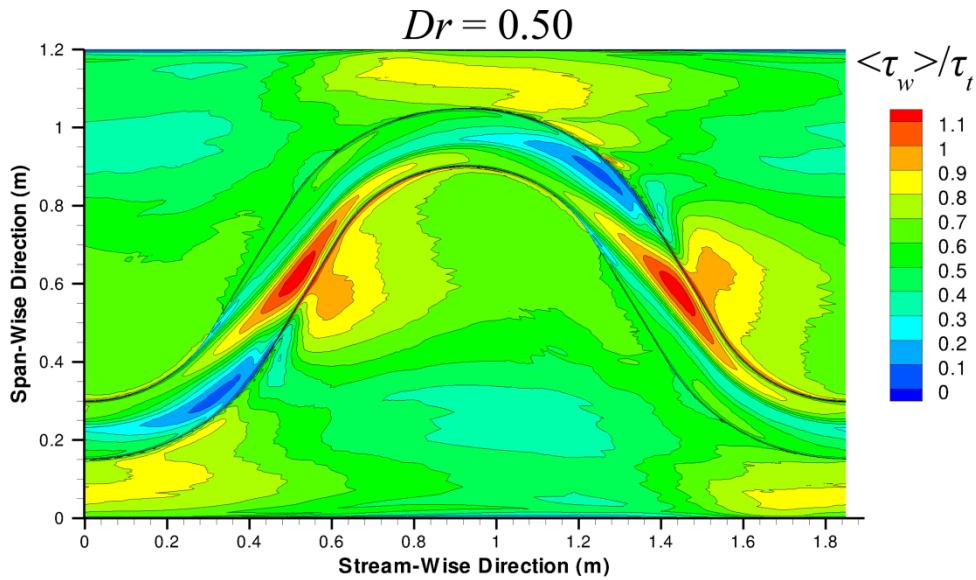
16
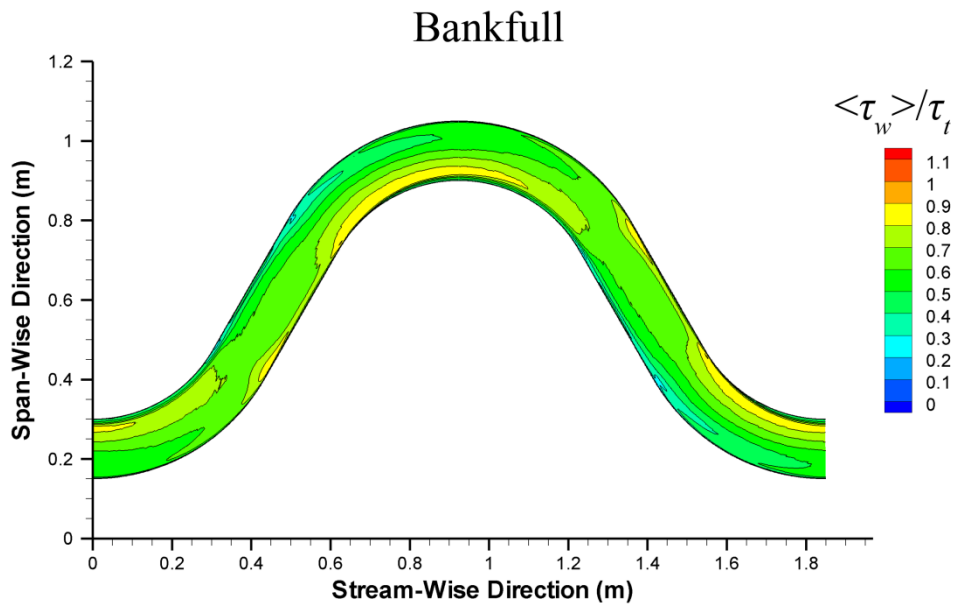
17
18 **Fig. 16.** Normalized bed shear stress τ ($\langle\tau_w\rangle/\tau_t$) for LES simulation: Bankfull case. (*Color*
19 *should be used in print*) (*1.5-colum fitting image*)
20

Fig. 17. Normalized bed shear stress ($\langle \tau_w \rangle / \tau_t$) for LES simulation: $Dr = 0.15$ case. (*Color should be used in print*) (*1.5-colum fitting image*)

Fig. 18. Normalized bed shear stress ($\langle \tau_w \rangle / \tau_t$) for LES simulation: $Dr = 0.15$ case. (*Color should be used in print*) (*1.5-colum fitting image*)

In order to provide a more quantitative comparison between the cases, Figure 19 shows profiles of the normalized bed shear stress distributions at the crossover region and the first half of the second bend (i.e Sections No. 03, 05, 07 and 09) for all three simulated cases. In the case of the Bankfull flow, coinciding with the maximum value of the streamwise velocity (Fig. 3, top panels), the maximum value of $0.87 \tau_t$ is reached at the beginning of the second bend (Section No. 09) near the inner wall. Except in Section No. 03, higher values are kept near the right bank all over the meander. Regarding the $Dr = 0.15$ case, the maximum value of $2.42 \tau_t$ is reached at the end of the first bend (Section No. 05) near the right bank, at the floodplain edge region. Similar feature ($2.27 \tau_t$) was found in Section No. 03. This high shear stress coincides with the

29

water ejection (contraction process) towards the flood plain in the outer part of the curve. Moreover, it might be related to the recirculation described above (Fig. 15) and therefore to the erosion mechanisms and channel migration. In the other sections of this shallow flooding case, higher values are always located near the right bank, at the floodplain edge region. The latter coincides with the the flood plain flow crossing over the main channel flow in the crossover region when it surpasses the right bank. Similar to the Bankfull case, in the main channel area, higher values are kept near the right bank throughout the meander (except in Section No. 03).

Finally, for the $Dr = 0.50$ the maximum value of $1.49\,\tau_t$ is reached in the crossover region (Section No. 07) near the right bank, at the floodplain edge region. The last phenomenon coincides with the the flood plain flow crossing over the main channel flow in the crossover region when it surpasses the right bank. Although the higher values are located in this case in a thin layer of the floodplain edge region, similar high values are also found in the main channel bed, although its extension is greater. Along the same main channel bed, its shear profile describes a shape very diffent from the Bankfull and $Dr = 0.15$ cases. In the deeper flow case there is a sinusoidal profile, which maximum values seems to be related to the center of the primary vortex (Fig. 11) throughout the meander. This relates to the aforementioned deep scour area (Wormleaton and Ewunetu, 2006), caused by such strong shear-driven vortex in the crossover region.
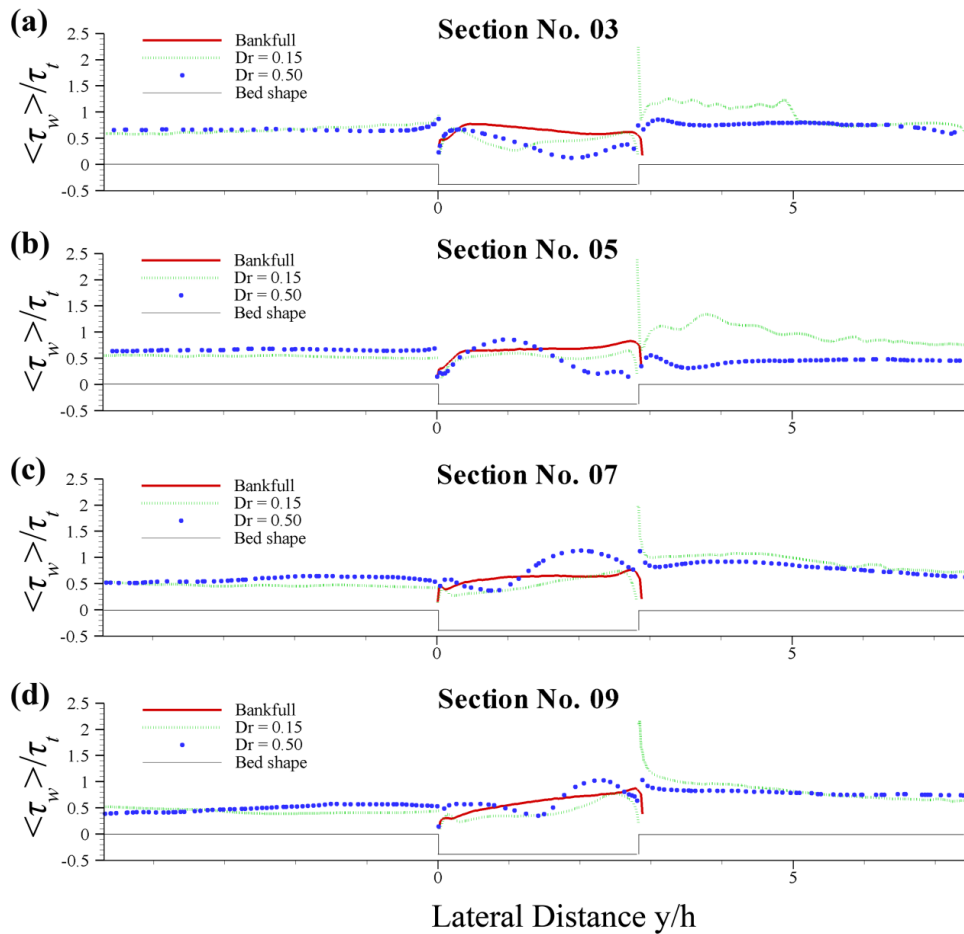
Fig. 19. Normalized bed shear stress ($\langle \tau_w \rangle / \tau_t$) profiles for LES simulations: (a) Section No. 05, (b) Section No. 07, (c) Section No. 09, (d) Section No. 011. (*Colour should be used in print*)
(*1.5-colum fitting image*)

1   ## 4.6   *Implications in Natural Banks*

2   The results presented in this paper have been obtained for a flow configuration which can be

3   considered as artificial. The present meander cross-section is rectangular and the ratio of width

4   to bankfull depth is about three. On the contrary, banks usually found in nature have irregular

5   cross-sections and are somewhat wider than the one studied here. In this context, it is worth

6   considering how representative the investigated configuration is for natural compound

7   meandering rivers.

8   First, secondary flow structures in the present configuration have an opposite sense of rotation

9   of the primary vortex at bend apices before and after inundation. This is consistent with the

10   secondary flows observed by Spooner (2001) who conducted experiments on a meandering

11   compound channel with natural bed forms, including mobile bed cases. A similar secondary

12   flow structure was reported by Wormleaton et al. (2004) who studied experimentally the flow in

13   a realistic main channel plan-form and dimensions, foodplain conditions and mobile bed. The

14   configuration may be considered as broadly representative of conditions that occur in natural

15   rivers. In the case of smooth floodplain, the flood plain flow created a strong vortex in the

16   crossover region which basically cancelled out the centrifugal circulation around the following

17   apex.

18   Concerning the horizontal turbulent shear layer, it has been shown that it is induced by the flood

19   plain flow crossing over the main channel flow in the crossover region. The presence and

20   relevance of such a shear layer have been also discussed in the literature for natural banks. For

21   example, in the study of Wormleaton et al. (2004) mentioned above, this was identified as one

22   of the main governing mechanisms for overbank flows. Moreover, Mera et al. (2014) and Mera

23   et al. (2015) performed experiments on a 1:20 physical Froude model of a real reach in River

24   Mero (Spain), for two depth conditions ($Dr = 0.26$ and $Dr = 0.38$). These authors also identified

25   the generation of a shear layer at the horizontal interface.

26   The interaction between floodplain flow and meandering flow was also reported by Mera et al.

27   (2015). In their study, they showed that the flow below the bankfull level visibly followed the

28   direction of the main channel, whereas the flood plain flow tended to follow the floodplain

29   direction bank. A realigment of the water circulation throughout the meander was observed.

30   They concluded that fluid exchange between the flood plain flow and the meander channel leads

31   to secondary currents. All these observations are consistent with the flow structure reported in

32   the present investigation. However, as in experimental studies data is collected at a limited

33   number of specific locations, explaining the flow structures and the generation of secondary

34   cells have involved in previous experimental researches a certain amount of guesswork.

35   Nevertheless, in this work, the LES computations provide a complete picture of the flow field so

36   that a definitive explanation can be given concerning the origin, structure and development of

37   secondary flows along the meander channel (see Figs. 3-12). Similarly, it is possible to make a

38   unique explanation of the structure of the secondary flow together with the turbulent kinetic

39   energy in the meandering channel for indicating a clear relationship between both of them (see

40   Figs 13-15). This strong link between the secondary flow and the turbulent kinetic energy using

41   visualization of streamlines has helped us to understand clearly the flow mechanisms of the

42   interaction beetween the main meander channel and the floodplain.

43   Moreover, in terms of experimental works, since the bed shear stress is a difficult quantity to

44   measure, it has been only measured in particular sections of a meandering channel, as for

45   example in the work of Hooke (1975). Therefore, the understanding of the behaviour of the bed

shear stress in most important flow interaction areas is lacking in the literature. The present work illustrates its distribution in the whole meander channel and also around very specific areas between the main channel and the floodplain edge (Figs 16-18). Thus, this analysis helps to identify the areas where the bed shear stress is above or below the critical shear stress, hinting to the possible occurrence of bed erosion or sediment deposition respectively along the compound meandering channel. For example, Fig 18 shows clearly the areas of the bed erosion and sediment deposition if the critical shear stress is above or below τ_t for each case. Knowing such parameters and their interactions is crucial to understand their implication for water environmental management. For this reason, this identification can be used for designing the appropriate level of bank protection for water management to determine possible regions of high bed stresses, where erosion or gradual channel migration might be expected.

In summary, the previous discussion suggests that, to a certain extent, the physical mechanisms driving the flow in natural compound meandering channels are essentially the same as the ones reported in this study. As a consequence, it might be possible to employ the present results in a broader context for water management planning and strategy, at least in a qualitative way.

5 Concluding Remarks

In this paper, the results of large eddy simulations of the flow in a periodic compound meandering channel for overbank flow for three different depth conditions were presented. Depth conditions for the meander with the rectangular cross-section and straight floodplain banks were one in-bank case and two overbank cases. The comparison with experimental data of the contours of the mean streamwise velocity, mean secondary currents as well as velocity fluctuations in selected cross sections was satisfactory. The predicted mean flow angle to meandering channel profiles also showed very good agreement with the measurements.

Our main interest concerned the development of the secondary motions due to the interaction between the main channel flow and the floodplain flow, the behaviour of the bed shear stress and the turbulent kinetic energy as well as their possible implications for sediment deposition, risk erosion and meander formation. In the simulations, the distribution of the velocities could be determined throughout the computational domain while in the experiment only a few planes could be measured. The changes of the secondary flow mechanisms with increasing flooding were clarified. We have shown that, associated with the contraction process (escaping flow from the meander) around the junction between the main channel and the flood plain, a small recirculation pattern appears at the floodplain edge region. This recirculation, which might be related to the erosion mechanisms causing scour associated to this kind of flow, seemed to be bigger when the flood water depth increased. Moreover, for the $Dr = 0.15$ case, one interacting cell after the bend apex was formed that switched from one bend to the other, but opposite to what happens in the Bankfull case. After the switch from bend apex to apex, it is dissipated by the water intrusion from the floodplain (flow expansion process), on the other hand a new cell emerges, which is very relevant to turbulent transport and mixing along the meandering channel. In this sense, the phenomenon of flow expansion tended to weaken in the case of increased flooding. Then, the secondary flow structure with a primary gyre in the meander is almost completely controlled by the flood flow direction over the in-bank flow. We have also shown that, as the water depth grows, a shear layer between the flow in the flooding level and the flow throughout the meander is produced. This shear layer generates additional turbulence due to the interaction and the mixing process between the flooding flow and the meandering flow.

The bed shear stress along the bottom wall was also estimated as an application of the initial step in the erosion processes. In the case of shallow flooding, high values were found in the zones where there is a greater interaction between the meander flow and the floodplain flow, where there is a strong acceleration due to the contraction and expansion of the flow. In contrast, in the deep floodplain case, the influence of the stresses within the floodplain was much lower than in the shallow case. In this case, higher influence was found in the straight sections of the meander.

Despite the fact that the present configuration presents several differences with respect to natural flow configurations, a literature review has shown that the main mechanisms driving the flow in both cases seem to be essentially equivalent. Thus, this work is useful for a broad range of compound meandering rivers found in nature. This suggests that the results presented here might be used in a more general context, for the determination of regions where erosion might be initiated or where channel migration and sediment deposition can be expected.

6 References

Blanckaert, K., 2009. Saturation of curvature-induced secondary flow, energy losses, and turbulence in sharp open-channel bends: Laboratory experiments, analysis, and modeling. J. Geophys. Res. Earth Surf. 114, F03015. https://doi.org/10.1029/2008JF001137

Blanckaert, K., Graf, W.H., 2004. Momentum Transport in Sharp Open-Channel Bends. J. Hydraul. Eng. 130, 186–198. https://doi.org/10.1061/(ASCE)0733-9429(2004)130:3(186)

Boussinesq, J., 1868. Mémoire sur l'influence des frottements dans les mouvements reguliers des fluids. J Math Pures Appl 13, 377–424.

Breuer, M., Rodi, W., 1996. Large Eddy Simulation for Complex Turbulent Flows of Practical Interest, in: Hirschel, P.D.E.H. (Ed.), Flow Simulation with High-Performance Computers II, Notes on Numerical Fluid Mechanics (NNFM). Vieweg+Teubner Verlag, pp. 258–274. https://doi.org/10.1007/978-3-322-89849-4_19

Brevis, W., García-Villalba, M., Niño, Y., 2014. Experimental and large eddy simulation study of the flow developed by a sequence of lateral obstacles. Environ. Fluid Mech. 14, 873–893. https://doi.org/10.1007/s10652-013-9328-x

Carling, P.A., Cao, Z.X., Holland, M.J., Ervine, D.A., Babaeyan-Koopaei, K., 2002. Turbulent flow across a natural compound channel. Water Resour. Res. 38, 1270. https://doi.org/10.1029/2001WR000902

Chang, Y., 1971. Lateral mixing in meandering channels (Ph.D.). The University of Iowa.

Constantinescu, G., Kashyap, S., Tokyay, T., Rennie, C.D., Townsend, R.D., 2013. Hydrodynamic processes and sediment erosion mechanisms in an open channel bend of strong curvature with deformed bathymetry. J. Geophys. Res. Earth Surf. 118, 480–496. https://doi.org/10.1002/jgrf.20042

De Marchis, M., Napoli, E., 2008. The effect of geometrical parameters on the discharge capacity of meandering compound channels. Adv. Water Resour. 31, 1662–1673. https://doi.org/10.1016/j.advwatres.2008.07.014

Ervine, D.A., Sellin, R.H.J., Willetts, B.B., 1994. Large flow structures in meandering compound channels. Presented at the 2nd International Conference on River Flood Hydraulics, York, UK, pp. 459–469.

Hain, R., Kähler, C.J., Michaelis, D., 2008. Tomographic and time resolved PIV measurements on a finite cylinder mounted on a flat plate. Exp. Fluids 45, 715–724. https://doi.org/10.1007/s00348-008-0553-x

Hinterberger, C., 2004. Dreidimensionale und tiefengemittelte Large-Eddy-Simulation von Flachwasserströmungen (Ph.D.). University of Karlsruhe.

Hinterberger, C., Fröhlich, J., Rodi, W., 2007. Three-Dimensional and Depth-Averaged Large-Eddy Simulations of Some Shallow Water Flows. J. Hydraul. Eng. 133. https://doi.org/10.1061/(ASCE)0733-9429(2007)133:8(857)

Hooke, R.L.B., 1975. Distribution of Sediment Transport and Shear Stress in a Meander Bend. J. Geol. 83, 543–565. https://doi.org/10.1086/628140

Imamoto, H., Fujii, R., 1975. On the characteristics of an open channel flow through passage of cross-section (1) (Annuals No. 18B). DPRI, Kyoto Univ.

Jing, H., Guo, Y., Li, C., Zhang, J., 2009. Three-dimensional numerical simulation of compound meandering open channel flow by the Reynolds stress model. Int. J. Numer. Methods Fluids 59, 927–943. https://doi.org/10.1002/fld.1855

Julien, P.Y., Duan, J.G., 2005. Numerical Simulation of the Inception of Channel Meandering. Earth Surf. Process. Landf. J. Br. Geomorphol. Res. Group 1093–1110.

Kiely, G., 1990. Overbank flow in meandering compound channels-the importantmechanisms, in: International Conference on River Flood Hydraulics. W. R. White. Chichester, England, John Wiley & Sons, Wallingford, UK, pp. 207–217.

Koseff, J.R., Street, R.L., 1984. The Lid-Driven Cavity Flow: A Synthesis of Qualitative and Quantitative Observations. J. Fluids Eng. 106.

Mera, I., Anta, J., Pena, E., 2014. Streamwise vorticity generation in a compound meandering channel. Crc Press-Taylor & Francis Group, Boca Raton.

Mera, I., Franca, M.J., Anta, J., Pena, E., 2015. Turbulence anisotropy in a compound meandering channel with different submergence conditions. Adv. Water Resour. 81, 142–151. https://doi.org/10.1016/j.advwatres.2014.10.012

Moncho-Esteve, I.J., Folke, F., García-Villalba, M., Palau-Salvador, G., 2017. Influence of the secondary motions on pollutant mixing in a meandering open channel flow. Environ. Fluid Mech. 1–20. https://doi.org/10.1007/s10652-017-9513-4

Moncho-Esteve, I.J., Palau-Salvador, G., Shiono, K., Muto, Y., 2010. Turbulent structures in the flow through compound meandering channels, in: River Flow 2010 - Dittrich, Koll, Aberle & Geisenhainer (Eds).

Morvan, H., Pender, G., Wright, N.G., Ervine, D.A., 2002. Three-Dimensional Hydrodynamics of Meandering Compound Channels. J. Hydraul. Eng. 128, 674–682. https://doi.org/10.1061/(ASCE)0733-9429(2002)128:7(674)

Muto, Y., 1997. Turbulent flow in two-stage meandering channels (Ph.D.). The University of Bradford.

Palau-Salvador, G., Stoesser, T., Fröhlich, J., Kappler, M., Rodi, W., 2010. Large Eddy Simulations and Experiments of Flow Around Finite-Height Cylinders. Flow Turbul. Combust. 84, 239. https://doi.org/10.1007/s10494-009-9232-0

Rhie, C.M., Chow, W.L., 1983. Numerical study of the turbulent flow past an airfoil with trailing edge separation. AIAA J. 21, 1525–1532. https://doi.org/10.2514/3.8284

Sellin, R.H.J., Ervine, D.A., Willetts, B.B., 1993. Behaviour of meandering two-stage channels. Proc. Inst. Civ. Eng. - Water Marit. Energy 101, 99–111. https://doi.org/10.1680/iwtme.1993.23591

Shan, Y., Liu, C., Luo, M., Yang, K., 2016. A simple method for estimating bed shear stress in smooth and vegetated compound channels. J. Hydrodyn. 28, 497–505. https://doi.org/10.1016/S1001-6058(16)60654-6

Shiono, K., Chan, T.L., Spooner, J., Rameshwaran, P., Chandler, J.H., 2009a. The effect of floodplain roughness on flow structures, bedforms and sediment transport rates in meandering channels with overbank flows: Part I. J. Hydraul. Res. 47, 5–19.

Shiono, K., Chan, T.L., Spooner, J., Rameshwaran, P., Chandler, J.H., 2009b. The effect of floodplain roughness on flow structures, bedforms and sediment transport rates in meandering channels with overbank flows: Part II. J. Hydraul. Res. 47, 20–28.

Shiono, K., Muto, Y., 1998. Complex flow mechanisms in compound meandering channels with overbank flow. J. Fluid Mech. 376, 221–261. https://doi.org/10.1017/S0022112098002869

Shiono, K., Spooner, J., Chan, T., Rameshwaran, P., Chandler, J., 2008. Flow characteristics in meandering channels with non-mobile and mobile beds for overbank flows. J. Hydraul. Res. 46, 113–132.

Shukla, D.R., Shiono, K., 2008. CFD modelling of meandering channel during floods. Proc. Inst. Civ. Eng.-Water Manag. 161, 1–12. https://doi.org/10.1680/wama.2008.161.1.1

Smagorinsky, J., 1963. General circulation experiments with the primitive equations. Mon. Weather Rev. 91, 99–164. https://doi.org/10.1175/1520-0493(1963)091<0099:GCEWTP>2.3.CO;2

Stoesser, T., Braun, C., García-Villalba, M., Rodi, W., 2008. Turbulence structures in flow over two-dimensional dunes. J. Hydraul. Eng. 134, 42–55.

Stone, H., 1968. Iterative Solution of Implicit Approximations of Multidimensional Partial Differential Equations. SIAM J. Numer. Anal. 5, 530–558. https://doi.org/10.1137/0705044

Thomson, J., 1876. On the origin of windings of rivers in alluvial plains, with remarks on the flow of water round bends in pipes. Proc. R. Soc. Lond. 25, 5–8.

Van Balen, W., Blanckaert, K., Uijttewaal, W.S.J., 2010. Analysis of the role of turbulence in curved open-channel flow at different water depths by means of experiments, LES and RANS. J. Turbul. 11, N12. https://doi.org/10.1080/14685241003789404

Weitbrecht, V., 2004. Influence of dead-water zones on dispersive mass transport in rivers (PhD thesis). University of Karlsruhe, Institut for Hydrodynamics.

Werner, H., Wengle, H., 1993. Large-Eddy Simulation of Turbulent Flow Over and Around a Cube in a Plate Channel, in: Durst, F., Friedrich, R., Launder, B.E., Schmidt, F.W., Schumann, U., Whitelaw, J.H. (Eds.), Turbulent Shear Flows 8. Springer Berlin Heidelberg, pp. 155–168. https://doi.org/10.1007/978-3-642-77674-8_12

Wormleaton, P.R., Ewunetu, M., 2006. Three-dimensional k-epsilon numerical modelling of overbank flow in a mobile bed meandering channel with floodplains of different depth, roughness and planform. J. Hydraul. Res. 44, 18–32.

Wormleaton, P.R., Sellin, R.H.J., Bryant, T., Loveless, J.H., Hey, R.D., Catmur, S.E., 2004. Flow structures in a two-stage channel with a mobile bed. J. Hydraul. Res. 42, 145–162.

Xie, Z., Lin, B., Falconer, R.A., 2013. Large-eddy simulation of the turbulent structure in compound open-channel flows. Adv. Water Resour. 53, 66–75. https://doi.org/10.1016/j.advwatres.2012.10.009

Xu, D., Bai, Y., Munjiza, A., Avital, E., Williams, J., 2013. Investigation on the Characteristics of Turbulent Flow in a Meandering Open Channel Bend Using Large Eddy Simulation, in: Proceedings of 2013 IAHR World Congress.